TAMPEREEN TEKNILLINEN YLIOPISTO
TAMPERE UNIVERSITY OF TECHNOLOGY

NINA HEIKKILÄ

INFLUENCE OF AMBIENT WORKING CONDITIONS ON THE PERFORMANCE OF PLANAR AND MESOSCOPIC PEROVSKITE SOLAR CELL ARCHITECTURES

Master of Science Thesis

Examiners: D. Sc. (Tech) Paola Vivo and Adj. prof. Terttu Hukka
Examiners and topic approved by the Dean of the Faculty of Natural Sciences on 1st of March 2017

ABSTRACT

NINA HEIKKILÄ: Influence of Ambient Working Conditions on the Performance of Planar and Mesoscopic Perovskite Solar Cell Architectures
Tampere University of Technology
Master of Science Thesis, 63 pages, 2 Appendix pages
March 2017
Master's Degree Program in Science and Engineering
Major: Chemistry
Examiners: D.Sc. (Tech.) Paola Vivo and Adjunct professor, University Lecturer Terttu Hukka

Keywords: perovskite solar cell, planar, mesoscopic, compact layer, ambient air, glove box, multi cation perovskite.

Perovskite solar cells can lower the price of the commercial solar cells by half compared to current silicon solar cells, and their research has skyrocketed during the recent years. In only seven years of research, their performance has exceeded 20 %, which makes them the fastest growing photovoltaic technology ever.

The main obstacle to the commercialization of the perovskite solar cells is their low stability. The active, light absorbing perovskite material starts to degrade under the influence of light, heat, humidity, and air, decreasing the device performance remarkably. The stability and the device performance of the cells have been improved by optimizing the cell structure, and by replacing the most commonly used perovskite material, $CH_3NH_3PbI_3$, with multi cation perovskites. In spite of the improved cell stabilities, the most efficient cells are still made in glove box in inert conditions under nitrogen gas.

In this Thesis, the influence of oxygen and humidity on the cell fabrication, on the cell performance, namely the cell efficiency and stability, was systematically studied. The influence was investigated for mesoscopic and planar cell architectures using both $CH_3NH_3PbI_3$ and multi cation perovskite, and two different electron transport materials, SnO_2, and TiO_2. The performance of the fabricated cells was compared to the data available in the literature for the state-of-the art solar cells, and to those of the devices fabricated at the University of Cologne in inert conditions. The cell performance was analysed quantitatively and qualitatively with IV measurement and SEM characterization, respectively.

The cells with triple cation perovskite produced twice as high efficiencies as the cells with $CH_3NH_3PbI_3$. The best device achieved an efficiency of 9.88 %, which is still far from the state-of-the art cells fabricated in glove box (> 20 %). The fabrication of electron transport layer in the ambient conditions had no influence on the cell performance. On the other hand, the crystallization of perovskite layer was crucially affected by the ambient conditions.

TIIVISTELMÄ

NINA HEIKKILÄ: Ympäröivien olosuhteiden vaikutus perovskiittiaurinkokennojen suorituskykyyn taso- ja mesorakenteisten kennojen valmistuksessa
Tampereen teknillinen yliopisto
Diplomityö, 63 sivua, 2 liitesivua
Maaliskuu 2017
Teknis-luonnontieteellinen tutkinto-ohjelma
Pääaine: Kemia
Tarkastajat: TkT Paola Vivo ja dosentti, yliopistonlehtori Terttu Hukka

Avainsanat: perovskiittiaurinkokenno, tasorakenne, mesorakenne, hapelliset olosuhteet, monikationiset perovskiitit

Perovskiittiaurinkokennot voivat laskea kaupallisten aurinkokennojen hintaa jopa puoleen nykyisestä ja niiden kehitys on kasvanut räjähdysmäisesti viime vuosien aikana. Vain seitsemän vuoden tutkimuksen aikana niiden hyötysuhde on ylittänyt 20 %, mikä tekee perovskiittikennoista historian nopeimmin kehittyneen valosähköisen sovelluksen.

Suurimpana esteenä perovskiittikennojen kaupallistamiselle on niiden heikko stabiilisuus. Kennon aktiivinen, valoa absorboiva perovskiittimateriaali alkaa hajota valon, lämmön, kosteuden ja hapen läsnä ollessa, mikä alentaa kennon tehokkuutta merkittävästi. Kennojen stabiilisuutta ja tehokkuutta on parannettu kennon rakenteen optimoinnilla ja korvaamalla yleisimmin käytetty perovskiittimateriaali, $CH_3NH_3PbI_3$, monikationisilla perovskiittimateriaaleilla. Kennojen stabiiliuden parantumisesta huolimatta, tehokkaimmat kennot valmistetaan edelleen inerteissä olosuhteissa typpihansikaskaapissa.

Tässä diplomityössä tutkittiin hapen ja kosteuden vaikutuksia kennojen tehokkuuteen ja stabiilisuuteen, systemaattisesti kennojen eri valmistusvaiheissa. Vaikutuksia tutkittiin meso- ja tasorakenteisilla kennoilla käyttämällä sekä $CH_3NH_3PbI_3$, että monikationista perovskiittia ja kahta eri elektroninkuljettajamateriaalia, TiO_2:a ja SnO_2:a. Valmistettujen kennojen suorituskykyä verrattiin tämän hetken tehokkaimpien kennojen kirjallisuusarvoihin ja Kölnin Yliopistossa, inerteissä olosuhteissa valmistettuihin kennoihin. Kennojen toimintaa analysoitiin kvantitatiivisesti virta-jännite -mittauksilla sekä kvalitatiivisesti SEM mittauksilla.

Monikationisen perovskiitin huomattiin parantavan kennojen hyötysuhdetta yli kaksinkertaiseksi $CH_3NH_3PbI_3$:a sisältäviin kennoihin verrattuna. Tehokkain hapellisissa olosuhteissa valmistettu kenno saavutti jopa 9.88 % hyötysuhteen, mikä on kuitenkin kaukana nykypäivän tehokkaiden kennojen hyötysuhteista (> 20 %). Elektroninkuljetusmateriaalin valmistusolosuhteilla ei huomattu olevan vaikutusta kennon tehokkuuteen. Perovskiitin valmistusvaiheen todettiin olevan vahvasti riippuvainen valmistusolosuhteista.

PREFACE

This Thesis was performed under the supervision of Dr. Paola Vivo. The Thesis was executed in the Laboratory of Chemistry and Bioengineering in Tampere University of Technology. The Thesis was examined by D.Sc. Vivo and adjunct professor Terttu Hukka. The Thesis key-results will be disseminated via poster presentation at the International Conference on Hybrid and Organic Photovoltaics (HOPV 17) in May 2017. The participation and travel to the conference is funded by the Finnish Cultural Foundation. I also wish to thank the Laboratory of Chemistry and Bioengineering for providing financial support for purchasing the chemicals for the experimental work.

I would like to thank D.Sc. Vivo for her valuable guidance and encouragement with the experiments, throughout the writing process, and admirable interest on the research subject. I would also like to thank adjunct professor Hukka for introducing me to the field of solar cells, and her precise examination on the writing of the Thesis. I want to express my great gratitude to AK Mathur group led by Prof.Dr. Sanjay Mathur, and especially M.Sc. Senol Öz, M.Sc. Eunhawn Jung, and M.Sc. Alexander Möllman, for their crucial help and experiments executed in the University of Cologne.

I want to thank M.Sc. Arto Hiltunen and M.Sc. Tero-Petri Ruoko for their extremely valuable help and guidance, especially with IV measurements, throughout the Thesis. I also want to thank M.Sc. Hiltunen and D.Sc. (Tech) Hanna Hakola for their crucial help with the SEM measurements.

Last, but not least, I want to express my great gratitude to my beloved boyfriend, my family, and friends, for their endless support during my studies, and working with this Thesis. Without you I could not had done this.

Tampere, 22.3.2017

Nina Heikkilä

CONTENTS

LIST OF SYMBOLS AND ABBREVIATIONS

AM	Air Mass
ALD	Atomic Layer Deposition
CBD	Chemical Bath Deposition
Cs/MA/FA	Triple Cation Perovskite with Cesium, Methylammonium and Formamidinium Cations
c	Speed of Light in Vacuum
DMSO	Dimethyl Sulfoxide
DMF	Dimethylformamide
DSSC	Dye-Sensitized Solar Cell
ETL	Electron Transport Layer
ETM	Electron Transport Material
EQE	External Quantum Efficiency
FA	Formamidinium Cation
FF	Fill Factor
FK209	Tris(bis(trifluoromethylsulfonyl)imide)
FTO	Fluorine Doped Tin Oxide
h	Planck's Constant
HOMO	Highest Occupied Molecular Orbital
HTL	Hole Transport Layer
HTM	Hole Transport Material
IV	Current-Voltage
J_{sc}	Short Circuit Current
Li-TSFI	Bis(trifluoromethane)sulfonimide lithium salt
LUMO	Lowest Unoccupied Molecular Orbital
MA	Methylammonium Cation
MPP	Maximum Power Point
r	Ionic Radii
P_m	Maximum Power
PCBM	[6,6]-Phenyl C_{61} butyric acid methyl ester
PCE	Power Conversion Efficiency
PSC	Perovskite Solar Cell
PSSC	Perovskite Sensitized Solar Cell
PV	Photovoltaic
SEM	Scanning Electron Microscopy
Spiro-OMeTAD	$N^2,N^2,N^{2'},N^{2'},N^7,N^7,N^{7'},N^{7'}$-octakis(4-methoxyphenyl)-9,9′-spirobi[9H-fluorene]-2,2′,7,7′-tetramine
t	Tolerance Factor
TUT	Tampere University of Technology
UVO	Ultraviolet-Ozone Surface Treatment
V_{oc}	Open Circuit Voltage

1. INTRODUCTION

World energy demand has been estimated to increase by 40 % by the year 2035, thus fulfilling the energy need is one of the most challenging aims of technology and research [1, p. 3]. Photovoltaics are an attractive solution to this problem since solar energy is world's biggest energy resource: every minute enough sunlight reaches the Earth to meet the energy need for the whole planet for one year. However, only 1 % of the electric energy on the Earth is produced by solar energy. The most common solar cells commercially available are today made of crystal structured silicon. These silicon cells have been in the solar cell markets for 50 years and their development has been very slow. Present commercial silicon structured solar cells provide on average ~15 % power conversion efficiency (PCE), and their manufacture is rather expensive. [2, 3]

Perovskite solar cells (PSCs), among other third generation solar cells, pursue high efficiency and low manufacture costs. Their desired features include flexibility and transparency, which make third generation solar cells suitable for a wide variety of novel applications of photovoltaic technology, e.g. building integrated photovoltaics, intelligent packaging and wearable devices. Being organic-inorganic hybrid devices, PSCs allow combining the typical features of inorganic materials, such as the great mobility of charge carriers, great stability and easily compatible manufacture methods, with those of organic materials, such as convertible absorption capacity and the facile material treatment. [2]

It has been calculated that PSCs can remarkably reduce the costs of solar cell production, potentially lowering them to half of the corresponding costs of traditional silicon solar cells. PSCs have been the fastest advanced photovoltaic device ever: in only seven years, their PCE has increased from 9.7 % (2009) to 22.1 % (2016). [2, 4] The most commonly applied PSC architectures are mesoscopic and planar PSCs. State-of-the-art PSCs are fabricated in inert environment in glove box due to perovskites' remarkable sensitivity to light, oxygen, heat and moisture. The purpose of this work is to examine the influences of ambient fabrication conditions compared to the cells fabricated in the glovebox. The cells are fabricated in ISO 6 clean room at ~45 % relative humidity and ~21 °C temperature, indicated as ambient working conditions throughout this work. The performance and the fabrication processes are compared to reference cells fabricated in glove box from the latest articles and with the corresponding devices fabricated at the University of Cologne. Both mesoscopic and planar cell architectures are investigated.

The different fabrication methods include two step sequential deposition of methylammonium lead iodide, $MAPbI_3$ and one step antisolvent methods of $MAPbI_3$ and Cs/MA/FA

triple cation perovskite. Two different compact layers, namely TiO_2 and SnO_2, are separately applied to all the different cell structures under investigation. These two compact layers and the two perovskite structures are applied to the record cells of today, and thus show superior qualities in the cell performance. The quality of the fabricated compact layers is also validated by collaborating with AK Mathur group at the University of Cologne. Samples with both SnO_2 and TiO_2 compact layers, in mesoscopic and planar structures, are fabricated in glove box and analyzed at the University of Cologne.

It is worth noting that, while the reported PSCs in literature are rarely fabricated in ambient conditions, the work aims to understand if the glove box is necessary for fabricating high efficiency perovskite solar cells. By examining the compact layers fabricated in ambient air in inert conditions the possible necessity of glovebox in the cell fabrication can more closely be pointed to the fabrication step of the compact layer or to the fabrication step of the perovskite layer. The cell performance is evaluated by current-voltage (IV) measurement and scanning electron microscope (SEM) imaging. Ageing of the best performing cells is also investigated.

Chapter 2 covers the fundamental physics of the solar cell functioning from the photovoltaic effect to the electron excitation in the molecule and light absorption in semiconductor materials. Furthermore, the main parameters for solar cell characterization and charge transport in the cell are discussed. Chapter 3 gives a detailed illustration of perovskite materials, presents the different layers in the cells and the cell architectures. The cell fabrication and characterization methods are discussed in chapter 4 and finally the results are presented in chapter 5. In chapter 6, the main results are summarized and the possible future studies are suggested.

2. THEORETICAL BACKGROUND

The working principles of solar cells are the light absorption of the active material followed by the formation of mobile charge carriers that transport the charges to the electrodes. The charge carriers are finally conveyed to an external circuit to produce electricity. [1, p. 430] In this chapter, the fundamental principles of solar cell operation are introduced.

2.1 Fundamental Physics Behind the Solar Cells

The energy of a photon is given as follows

$$E = \frac{hc}{\lambda} \qquad (1)$$

where λ is the wavelength of the photon in meters, h is Planck's constant and c is the speed of light in vacuum. The energy of the photon is usually given in electron-volts rather than in Joules, since the energy is very small. From equation 1, we can deduce that a photon with a short wavelength has a higher energy compared to a photon with a high wavelength. The wavelength of the visible light corresponds to a different color according to the light visible spectrum. The lowest wavelengths of the visible light range are around 400 nm (blue color), while the highest wavelengths are around 750 nm (red color). The energy corresponding to blue light at 400 nm is about 3.2 eV. When shifting to higher wavelengths the energy decreases. At 750 nm, the corresponding energy of the photon is 1.7 eV which is nearly half of the photon with wavelength of 400 nm. [5, pp. 5–6]

The photovoltaic effect describes the transfer of charges, e.g. electrons in metal surfaces. Light incident on a metal plate can be absorbed leading to the excitation of electrons to unoccupied energy levels. If the electron gains sufficient amount of energy it will be emitted from the metal surface and can be collected on another metal surface in the surrounding system called collector. [6, p. 279] This is the fundamental phenomenon behind the photovoltaic (PV) devices.

If two atoms are brought close together, a mutual coupling of atoms occur. This results a change in energy conditions and each discrete energy level for an electron divides into two individual states. This can be thought as an example of harmonic oscillators. If a harmonic oscillator is coupled, the result are two new resonance frequencies. In a semiconductor crystalline material, there are infinite number of atoms that can couple together. The result is an infinite number of individual energy levels which are hardly recognizable. These levels form energy bands and they include all the energy states allowed for an electron. Valence band is the highest occupied band or molecular orbital (HOMO), and the conduction band is the lowest unoccupied band or molecular orbital (LUMO). The

zone between the two bands is the forbidden zone that an electron must overcome to excite; the width of the forbidden zone is called bandgap. When the electron is excited to the conduction band or LUMO level, the electron becomes a conductor electron, which increases the conductivity of the material. Insulators, semiconductors and conductors can be classified according to their bandgaps. For insulators the bandgap is rather big, typically over 3 eV which means that there are nearly any free electrons available even at high temperatures. For semiconductors the bandgap is typically in the region between 3 eV and 0 eV and for conductors the valence and conduction bands overlap, indicating a high degree of conductivity even at low temperatures. [7, pp. 47−49] As a general rule, the narrower the bandgap of a material, the better are its conducting properties. Hence, in order to harvest as many solar photons as possible, the bandgap of the semiconductor should be minimized. [8, p. 56]

When the electron is released from the HOMO level, a gap in the crystal structure occurs. This gap forms a hole in the structure and the process is electron-hole pair generation. The narrower the band gap is the higher the electron-hole generation rate is [8, p. 56]. When the free electron returns from LUMO to HOMO level, the hole is filled and this is called electron-hole pair recombination. The generation and recombination of electron-hole pairs occurs continuously in the crystal resulting an average number of free electrons and holes in the material. The average number of electrons and holes in the structure is the carrier concentration. [7, pp. 49−50]

Imperfection recombination occurs when ideal crystal structure is imperfect, e.g. due to foreign atoms or crystal defects like empty lattices or crystal displacements. These imperfections create additional levels to the forbidden area between HOMO and LUMO levels. Additional levels act as step levels for electrons and make returning to the HOMO level simpler and more probable thus leading to increased recombination. Foreign atoms create recombination centers in the crystal structure called traps. [7, pp. 70−71] For PV applications, the recombination of charges is unfavorable since it decreases the carrier concentration and thus hinders the current flow. The crystals in high efficiency solar cells should be with high degree of purity in order to avoid remarkable recombination.

In the molecular lattice, the electrons of the outer atoms remain as open bonds since they have no bonding partners leading to undesired surface recombination. When considering the crystal surface, it becomes clear that the crystal structure of the active material on solar cell should be single crystalline. The material should also provide long carrier lifetimes and diffusion lengths. Carrier lifetime defines the average lifetime of the generated electrons before recombination. Diffusion length describes the distance the generated electrons travel before recombination. [7, p. 71]

2.2 Light Absorption

The main carrier generation in solar cell originates from the absorption of light. When a photon enters the semiconductor, it generates electron-hole pairs in a thin layer specific for the used materials. [9, p. 39] The amount of photocurrent in the cell depends on the number of incident photons absorbed and the generated electron-hole pairs need to be separated and brought to contacts. Part of the incident irradiance arriving to the cell surface (E_0), is reflected (E_R), part is penetrated to the cell (E_1) and part of the penetrated irradiance is passing through the cell (E_2). The total absorbed irradiance in the cell (E_{Abs}) is the difference between E_1 and E_2. [7, pp. 73−74] The absorption of the photons in the cell is presented in Figure 1.

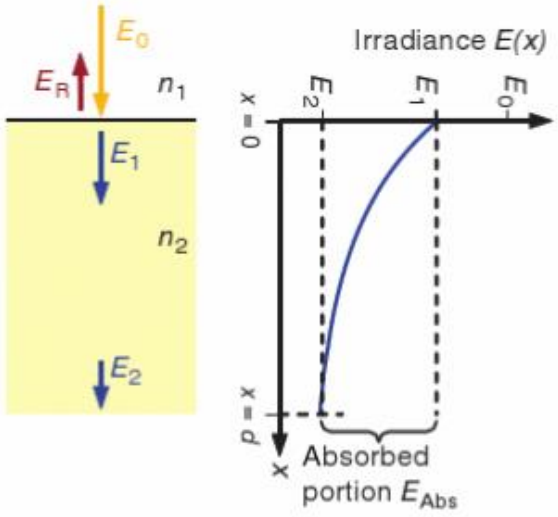

Figure 1. *Light absorption in solar cell. On the left is the energy diagram of the absorption and on the right is the schematic presentation of the irradiance absorption in the cell. In the diagram the vertical axis presents the penetration depth x and the horizontal axis presents the energy of the irradiance. d is the total thickness of the cell, E_0 is the energy of overall irradiance, E_R is the energy of irradiance reflected from the cell surface, E_1 is the amount of irradiance penetrated to the cell and E_2 is the amount of irradiance passing through the cell (adapted from Ref.[7, p. 74]]).*

The absorption efficiency η_{Abs} can be calculated as follows

$$\eta_{Abs} = \frac{E_{Abs}}{E_0} = \frac{E_1 - E_2}{E_0} \qquad (2)$$

and it is the relationship between the number of absorbed photons and the number of incident photons arriving the cell surface. If the amount of reflected irradiance is small, the absorption efficiency can reach values near to 100 %. The reflectance of the irradiance can be reduced e.g. by using anti-reflection layer on top of the cell. The cell thickness has an influence on the absorption since when the cell thickness *d* is as long as the penetration

depth *x* the amount of photons left over is minimum as can be seen in Figure 1. However, the absorption efficiency is also dependent on the wavelength of the photons and as depicted in chapter 2.1 photons with high wavelengths are absorbed relatively weakly and this would demand an effective cell to be relatively thick. For example, the infrared light with a wavelength 1000 nm and a cell thick enough for 1 % loss of photons would have a minimum thickness of approximately 900 μm which is very thick for photovoltaic devices. Thick cells are expensive to produce and the high thickness of the cell causes quantity of charge recombination on their way to the space charge region discussed in the next chapter. With the use of optical reflector in the back of the solar cell, the optical path distance can be doubled in the cell without raising the cell thickness. [7, pp. 74−75]

2.3 Charge Transportation

In organic solar cells, the absorption of photons creates excitons that are strongly bound electron-hole pairs and they are practically neutral on the outwards. For this reason, organic solar cells include dissociation surfaces where the excitons are separated. In inorganic solar cells, the exciton binding energy is relatively small and in the case of highly crystalline materials, like perovskites, the exciton binding energy is negligible and free charges form practically immediately after the absorption of the photon. Fast charge combination is advantage related to organic solar cells since the formation and dissociation of excitons require energy, which in turn has a negative influence on the cell performance. [10]

Semiconductors are poor electrical conductors which need to be doped by introducing foreign atoms into their crystal structures in order to make them sufficient electric conductors for PV applications. Doping the structure with an atom that easily donates free electrons to the crystal lattice is called n-doping. On the contrary, an atom that has have incomplete bonds can donate holes to the structure and this is called p-doping. Holes and free electrons can move in the crystal lattice creating a conduction. The reason why semiconductors are used in PV applications instead of conductors is that their features can be easily modified by n- and p-doping. Combining the p- and n-doped materials together creates a p-n junction where the free charges diffuse due to the concentration gradient. Finally, the free charges recombine with the holes or electrons in the opposite regions of the cell. In the junction area, there are almost no free charges that the fixed charges could compensate and the rising number of fixed charges in the junction area finally creates an electrical field. The electric field pushes the electrons to the n-doped region and the holes to the p-doped region creating a new balance where diffusion and field current cancel each other and a space charge region is present. Space charge region causes a potential difference through the region called diffusion voltage. [7, pp. 53−55]

When a voltage is applied to the p-n junction in the forward direction the electrons are driven into the n-region. In the p-n junction the electrons are however hindered to move into the p-region due to the space charge region field and the electrons back up at the

border of the region while reducing the charge region by neutralization of the positive fixed charges. The same behavior occurs also on the p-region with the holes and finally, when increasing the voltage the space charge region disappears completely and a current can flow. The voltage required for the current flow is the open circuit voltage, V_{oc}. When a reverse voltage is applied to the p-n junction, the space charge region is enlarged and only a minimal reverse current flows. [7, pp. 58]

The cell efficiency can be improved by manipulating the distance the charge carriers travel through the cells to the electrodes. High efficiency cells demand ideal charge carrier travel distances, which are affected by all the cell layers and their interfaces. [11] The interface between two different materials forms an electric heterojunction and its characteristics are dependent not only of the band gaps, but also the electron affinities and the ionization energies of both of the materials have influence on it [12]. High efficiency also requires excellent absorption ability, balanced charge transportation and long diffusion in perovskite layer [2].

2.4 Parameters for Solar Cell Characterization

Spectrum of light originating from the sun is called the solar irradiance. The solar irradiance can be standardized by the specific air mass (AM) spectrum. Air mass is ratio of the direct optical path length of solar irradiance through the Earth's atmosphere, L_θ, relative to the zenith path length, L.

$$AM = \frac{L}{L_\theta} \sim \frac{1}{\cos\theta} \tag{2}$$

θ is the zenith angle of incidence irradiance. Equation 2 gives the air mass at average sea level. For photovoltaic industry, the standardized air mass for solar cell characterization is AM 1.5 which refers to a 48.19° solar zenith angle. As can be deduced, the real solar irradiance depends strongly on the time of the day and month since the position of the sun is not constant. In addition, the composition of the atmosphere and the weather have an influence on the solar irradiance. [5, pp. 7−8] On a clear sunny day, a radiation value received to the Earth can be 1000 W/m^2. The standard test conditions for solar modules are defined for AM 1.5 and total irradiance of 1000 W/m^2 which is suitable for determining the peak power of a solar cell. [7, p. 24]

Most important factors when evaluating the effectiveness of solar cells are PCE, fill factor FF, short circuit current density J_{sc} and V_{oc} and these can be determined by measuring the current-voltage (IV) curve for the cell. A typical IV-curve measured for a solar cell is presented in Figure 2. The PCE for the cell can be calculated as

$$\mathrm{PCE} = \frac{P_m}{P_{in}} = \frac{J_m V_m}{P_{in}} = \frac{J_{sc} V_{oc} \mathrm{FF}}{P_{in}} \tag{3}$$

where P_m is the maximum power generated and J_m and V_m are corresponding current density and voltage for the P_m. P_{in} is the incident light power on the device. In Figure 2 P_m corresponds the power in maximum power point, M_{PP}. [12, 13] The theoretical limit of the solar cell is highly dependent of the bandgap of specific material. For example, methylammonium lead iodide, $MAPbI_3$ has an average bandgap of 1.55-1.60 eV and the corresponding maximum PCE would be 30-31 %. With a band gap between 1.1 and 1.4 eV the theoretical limit approaches to 33 %. For materials with higher bandgap, the theoretical PCE decreases almost linearly due to low photon harvesting. In the case of lower bandgaps, the voltage is low and most of the energy is lost due to thermalization thus leading to low PCEs. [8, p. 62]

FF characterizes the shape of the IV-curve measured for the cell and represents how difficult or easy the extraction of the photogenerated carriers is out of the solar cell. The FF can be seen in Figure 2, where it is presented as the lined area below the voltage axis. FF can be expressed in terms of P_m, J_{sc} and V_{oc} as follows

$$\mathrm{FF} = \frac{P_m}{J_{sc}V_{oc}} = \frac{J_m V_m}{J_{sc}V_{oc}} \qquad (4)$$

Ideal curve forms a rectangular area with the J- and V-axis and its FF is 1. In reality, the ideal FF is though never achieved because of physical limitations, thus the FF is always less than 1. The maximum FF reported for PV devices is about 90 %. [12, 13]

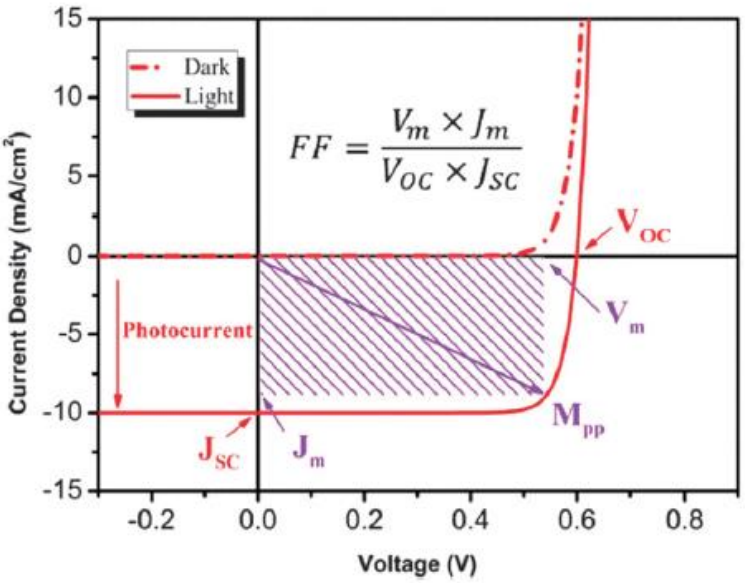

Figure 2. *Typical current-voltage curve measured for solar cell in dark (dashed line) and light (solid line). The most important parameters for cell characterization, FF, J_{sc} and V_{oc}, are illustrated in the picture. Also maximum power point M_{pp} and corresponding maximum current density J_m and voltage V_m for M_{PP} are presented (adapted from Ref. [13] with permission of Royal Society of Chemistry, Copyright 2013).*

Short circuit current is the highest current value at short circuit conditions (voltage across the cell is zero). J_{sc} is the short circuit current divided by the active area of the cell. As can be seen in the Figure 2 J_{sc} occurs when V_{oc} is zero and it is equal to the photocurrent. External quantum efficiency (EQE) is the ratio of the photogenerated electrons collected to the number of incident photons at specific wavelength. J_{sc} is directly related to EQE and it can be defined as:

$$J_{sc} = \frac{q}{hc}\int_{\lambda_{min}}^{\lambda_{max}} \mathrm{EQE} * P_{in}(\lambda)\lambda \, d\lambda \qquad (5)$$

where q is the elementary charge, P_{in} is the incident input power and λ_{max} and λ_{min} are the maximum and minimum wavelengths of the occurred photons. [12] The theoretical maximum J_{sc} for an ideal material is strongly dependent on the bandgap of the material as described also for the PCE before. For $MAPbI_3$ with bandgap of 1.55–1.6 eV the corresponding theoretical J_{sc} is about 25 mA cm^{-2}. With higher bandgaps, the J_{sc} decreases radically and on the contrary rises rapidly for lower bandgap values. [8, pp. 62−63]

V_{oc} is the maximum voltage a solar cell can provide to an external circuit. As can be seen in the Figure 2, V_{oc} occurs at the point where J_{sc} is zero. V_{oc} is presented as follows

$$V_{oc} = \frac{1}{q}\left(\left|E_{\mathrm{HOMO,D}}\right| - \left|E_{\mathrm{LUMO,A}}\right|\right) - 0.3\ \mathrm{V} \qquad (6)$$

where $E_{\mathrm{HOMO,D}}$ is the energy of the HOMO level of electron donor and $E_{\mathrm{LUMO,A}}$ is the energy of the LUMO level of the electron acceptor. The equation 6 is empirically derived by measuring the V_{oc} for several different devices, while keeping the acceptor material constant. The equation 6 suggests that the V_{oc} is directly proportional to the bandgap of heterojunction. The 0.3 V is the empirical loss factor. [12, 14]

3. PEROVSKITE SOLAR CELLS

Hybrid organic-inorganic perovskite materials were recognized as excellent semiconductor materials in the 1990's but they were not studied as absorbing agents in solar cells until 2009. [15] It was noticed that perovskite have excellent optical and electric properties. After that, the research on perovskite materials and their photovoltaic applications have been widely studied. In this chapter, different perovskite structures and the favorable qualifications for high efficiency perovskite solar cells are presented. In addition, different solar cell architectures and the constituents of the solar cell structures are introduced.

3.1 Perovskite Structure

Perovskite refers originally to inorganic, crystalline mineral and it has a common ideal formula of ABX_3. In the formula, A is a cation, B is usually a metal ion with a charge +2 like Pb^{2+}, Sn^{2+}, or Cu^{2+}, and X is a halide and usually Cl^-, Br^- or I^-. As usually, the overall structure must be electrically neutral. Small organic cations like $CH_3NH_3^+$ (methylammonium, MA), $C_2H_5NH_3^+$ (ethylammonium) and $HC(NH_2)_2^+$ (formamidinium, FA) can replace the inorganic A cation when the perovskite becomes an organic-inorganic hybrid material. [2] Cation A has +1 charge and it is the most important component of the perovskite molecule. The cation A determines the structure and the crystal size of perovskite and it directly influences the stability and optoelectronic properties of the perovskite. [16] In principle, an applicable molecular cation A has to be small enough not to break the three-dimensional perovskite network. On the other hand, the crystal properties become highly anisotropic and exciton binding energies become stronger when the charge carrier masses increase which are unfavorable properties in photovoltaic applications. [8, p. 2]

Perovskites exist in different cubic structures and they can have several different properties depending on the cubic and the molecular structure. For example, perovskites with insulating, semiconducting and superconducting properties are known. Perovskites are heteropolar crystals for which the stability is influenced by Madelung electrostatic potential. For group VII anions like halides, the electrostatic stabilization is weak, leading to low solid-state ionization potentials. This property is a desired feature for charge transfer materials, and makes halide perovskites suitable material for photovoltaic devices. [8, p. 2]

Perovskite has a generic cubic crystalline structure. In the three-dimensional cubic structure, the cations are located in the eight corners of the unit cells, and the cations are surrounded by 12 X anions. B cations are located in the middle of the unit cells and they are surrounded by six X anions forming $[BX_6]^{4-}$ octahedral. The three-dimensional cubic structure is presented in Figure 3.

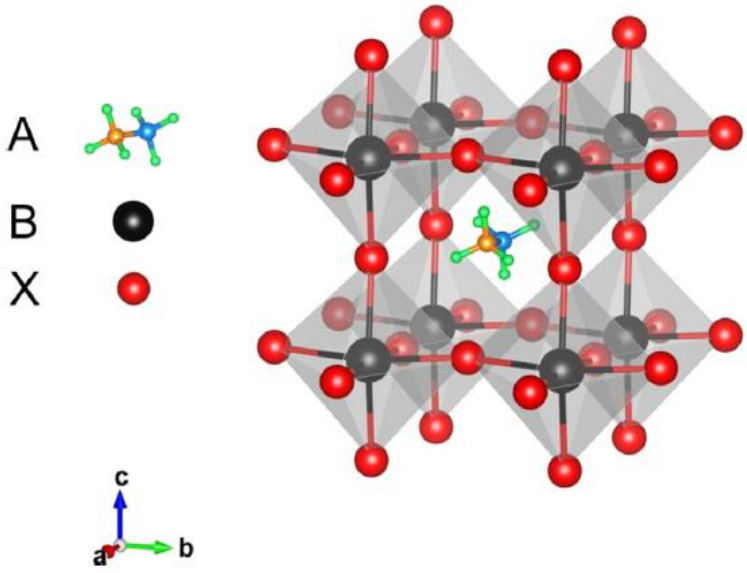

Figure 3. *Crystal structure of perovskite (adapted from Ref. [17] with permission of Elsevier, Copyright 2016).*

Ideal perovskite structure is inflexible. Since there are no adjustable atomic position parameters in the unit cell of perovskite all compositional changes would be adapted by a change in lattice parameter which is simply a sum of the bond lengths. As can be seen from Figure 3, the edge of the unit cell, *a*, is the B─X bond length times two:

$$2(B - X) = a \qquad (7)$$

The width of the three-dimensional octahedral cage site is two times the A─X bond length:

$$2(A - X) = \sqrt{2}a \qquad (8)$$

By dividing the equation 8 by equation 7, we get that the ideal crystal structure gives the ration for the bond lengths as follows

$$\frac{(A-X)}{(B-X)} = \sqrt{2} \qquad (9)$$

The equation 9 was figured by Goldschmidt, in 1926, to predict the probability of ions to form a perovskite structure phase. The equation 9 can be represented with respect to ionic radii, *r*, as follows

$$\frac{(r_A-r_X)}{(r_B-r_X)} = \sqrt{2} \qquad (10)$$

where r_A is the radius of cation A, r_B is the cation B and r_X is the radius of the anion. The equation 10 is called the Goldschmidt's rule and it can be represented with respect to tolerance factor, *t*

$$t = \frac{(r_A - r_X)}{\sqrt{2}(r_B - r_X)} = 1 \qquad (11)$$

Equation 11 represents that an ideal perovskite structure would have a tolerance factor 1. [18, pp. 6−10] The tolerance factor is a reasonable prediction for the perovskite structure to be formed. For perovskites it has been found that the cubic structure is typically formed when $0.78 < t < 1.05$. However, the perovskite structure has been argued not to be stable even for the most favorable tolerance factor range, which is between 0.8 and 0.9. This is why an additional factor needs to be considered to a more precise prediction for perovskite structure formation. Additional factor for this purpose is octahedral factor, μ, which can be represented as follows

$$\mu = \frac{r_B}{r_X} \qquad (12)$$

When determining the formability of alkali metal halide perovskites with t-μ mapping, the formation of perovskite is found in the region between $0.813 < t < 1.107$ and $0.442 < \mu < 0.895$. [19, pp. 244−246]

Perovskite materials have exceptional material properties resulting in high performance solar cells. These properties include a remarkably high absorption over the visible spectrum, low exciton binding energy, charge carrier diffusion lengths in the μm range, a sharp optical band edge and a tunable band gap by replacing the cations and anion in the molecule. These properties are introduced in the next chapter.

3.1.1 Single Cation Perovskites

The most widely studied perovskite material is $MAPbI_3$. The single cation perovskite refers here to the number of cation 'A' in the molecule. Accordingly, $MAPbI_3$ is a single cation perovskite. In organic-inorganic perovskites the $[PbI_6]^{4-}$ octahedral can form three-, two-, one- or zero-dimensional networks maintaining the same unit structure. [20] The simple or complex defects in $MAPbI_3$ lattice induce only shallow defect levels due to high formation energy of the cubic structure, which can partially explain the long exciton lifetimes and diffusion lengths. This can be derived from the fact that deep-level point defects cannot act as non-radiation recombination sites since they are absent in the structure. This may also clarify the large open-circuit voltage typically measured for these materials. [21] Large perovskite crystal grains with less grain boundaries in the layer have a positive influence on the charge lifetimes. Hence, the fabrication of homogenous and big crystals is needed for good devices performance [22].

In photovoltaic applications, the tuning of the physical properties and especially bandgap tuning is important in terms of spectral responsivity for optimal cell materials. The physical properties of $MAPbX_3$ can be tuned by substituting cation A or B. When substituting the cations in perovskite molecule, the cubic structure must be maintained. For example,

estimations of the optimal radii for cation A with respect to the effective ionic radii of two commonly used B anions, Pb^{2+} and Sn^{2+} and halide X are compared in Table 1. The estimations are calculated with two different tolerance factors, for t = 1.0 and for t = 0.8 to cover the most favorable formation region. According to the literature reference, the length of C—C bond is 150 pm and the length of C—N bond is 148 pm. In the range of estimations of Table 1, A can have one or two C—C or C—N bonds which partially explains the stabilization of MA in perovskite structure. [19, pp. 244−246]

Table 1. *Estimating the optimal radii for cation A in organo metal halide perovskite structure. In table B refers to anion in perovskite structure, X is the halide and r is the effective ionic radii. r_A is estimated from the equation (11). r_B for Pb_2^+ is 119 pm and 118 pm for Sn_2^+. r values are the r_X values for respective X. [19, p. 245]*

B	**X**	***r* [pm]**	**r_A [pm], t = 0,8**	**r_A [pm], t = 1,0**
Pb^{2+}	Cl^-	181	158.4	243.3
	Br^-	196	160.4	249.5
	I^-	220	163.5	259.4
Sn^{2+}	Cl^-	181	157.3	241.8
	Br^-	196	159.3	248.1
	I^-	220	162.4	258.0

As mentioned earlier, MA can be replaced by larger cations like ethylammoniun or formamidinium, FA, which has an ionic radii of approximately 190-220 pm and it is in the estimated range according to Table 1. [8, p. 226, 23, 24] The change of cation A from MA to ethylammonium or FA shifts the bandgap energy of the material due to structural modification. For $MAPbI_3$, the bandgap is expected to be around 1.52 eV and when MA is replaced with ethylammonium the resulting bandgap energy is 2.2 eV and for $FAPbI_3$ 1.45 eV. [19, p. 246] The band gap of $FAPbI_3$ is lower and thus closer to the single junction optimum compared to the band gap of $MAPbI_3$. This allows extended solar light harvesting efficiency. [25] The lower bandgap shifts the absorption spectrum edge from 800 nm for $MAPbI_3$ to 840 nm for $FAPbI_3$ enabling extended light harvesting [24]. $FAPbI_3$ has also found to obtain better thermal stability when compared to $MAPbI_3$. Nevertheless, the drawback of $FAPbI_3$ is the structural instability of the black perovskite phase at room temperature which results to conversion of the perovskite into a photoinactive hexagonal δ-phase, “yellow phase” which is also called nonperovskite. [26] The photoactive “black phase” is instead α-phase and it is sensitive to solvents or humidity. Generally, perovskites with t value in the desired range exhibit the black phase in room temperature and perovskites with lower t values exhibit yellow phases [27]. Cation A could also be replaced by inorganic cesium. The thermal stability of the $CsPbX_3$ is excellent and the band gap is highly dependent of the halide in the structure. For $CsPbI_3$ the band gap is 1.73 eV, which makes it suitable for photovoltaics but for the $CsPbBr_3$ the

band gap is somewhat higher, 2.25 eV and for this reason it is rather unfavorable. $CsPbI_3$ also shows good emissive properties but the photoactive black phase is unstable at temperatures lower than 300 °C. [25, 28]

Despite the vigorous research about the perovskite materials, the role of the organic cation in perovskite structure it is still not completely clear. Recent theoretical research have suggested that the only role of the organic cation A in the perovskite structure is to stabilize the perovskite structure electrostatically and A has no remarkable contribution to the electronic structure around the band edges. [21]

The replacement of halides in perovskite $MAPbX_3$ structure has been widely studied, leading to notable differences in the electrical behavior of the perovskite. When the tolerance factors for $MAPbX_3$ structure were calculated, the radii of the halide and Pb^{2+} were applied from the Table 1. For the radii of MA, 180 pm was used. For X = Cl^- we get 0.85, for Br^- 0.84, and for I^- 0.83. These results indicate that for most cubic perovskites the tolerance factor is in the region between $0.8 < t < 0.9$ which is in the region estimated in chapter 3.1. With these estimations, the $MAPbX_3$ perovskites is expected to crystallize in a cubic structure. [19, p. 246] The crystal structure can however experience temperature–dependent transformations even in inert atmosphere. [26] Three different phases, orthorhombic, tetragonal and cubic Bravais lattices, are identified for $MAPbI_3$ when gradually increasing the temperature. These three phases differ in enthalpy, three-dimensional position, and lattice parameters. [8, pp. 3−5]

Some of the essential physical properties of $MAPbX_3$ are presented in Table 2. As can be seen in the table, the dielectric constant increases and the bandgap energies decrease with respect to the increasing halogen ion size from Cl^- to I^-. Concerning the data in Table 2, we can conclude that $MAPbCl_3$ would be the worst choice of the three X options presented, due to its relatively larger bandgap when compared to $MAPbI_3$ and $MAPbBr_3$. The lowest bandgap for $MAPbI_3$ thus favors its usage as a semiconductor. $MAPbCl_3$ has the lowest dielectric constant indicating the lowest conductivity.

Table 2. *Physical properties of $MAPbX_3$ perovskites. X is the halogen in the molecule, ε is the dielectric constant, μ_m is the dipole moment and E is the experimentally determined bandgap for the cubic structure for each halogen in the molecule. [19, pp. 245−246]*

X	$\boldsymbol{\varepsilon}$	$\boldsymbol{\mu_m}$ **[D]**	$\boldsymbol{E}$ **[eV]**
Cl^-	23.9	0.850	2.34
Br^-	25.5	0.766	1.80
I^-	28.8	0.854	1.57

The mixing of different halides in the perovskite structure has led to significant improvement in cell performance and perovskite stabilization. It has been found that the increase

of the Br content in the perovskite material contributes considerably to thermal stability. [24, 25] However, $MAPbBr_xI_{3-x}$ perovskites have shown halide segregation, light-induced trap state formation, degradation upon contact with moisture and thermal instability [25]. When the charge transport properties of $MAPbI_3$ and $MAPbI_{3-x}Cl_x$ are compared, a notable difference in the charge diffusion lengths is observed. For $MAPbI_3$ the diffusion lengths for electron and hole diffusions are 130 nm and 100 nm, respectively, while for $MAPbI_{3-x}Cl_x$ the corresponding diffusion lengths are 1096 nm and 1213 nm in which also photo-induced free charge carriers are observed. The longer diffusion lengths and free charge carriers in $MAPbI_{3-x}Cl_x$ indicate the generation of weakly bound excitons by light illumination which in turn can lead to V_{oc}. [29] Furthermore $MAPbI_3$ has an ability to accumulate charges due to the high density of states. This phenomenon was not observed in any light absorbing material before, which strongly indicated that PSCs are different from the sensitized and inorganic thin film solar cells but rather a new kind of photovoltaic devices. [19, p. 248]

The most efficient PSCs today contain Pb anion on the B site but, since the water soluble Pb salts contained in the perovskite film are toxic upon human exposure and for environment, alternative anions are constantly researched. The divalent cation B in $MABI_3$ structure can be replaced for example with Sn^{2+} when the resulting bandgap 1.2 eV is narrower than the bandgap for Pb^{2+}, 1.5 eV. Reducing the bandgap influences the material emission wavelength, by shifting it from 750 nm to 1000 nm and thus enhancing the spectral responsivity. [19, p. 246] Theoretical studies have however shown that Pb^{2+} has a significant role in determining the perovskites' electronic structure, which creates big challenges in finding a good alternative for the Pb^{2+} anion without sacrificing the high performances achieved today. [30]

3.1.2 Mixed Cation Perovskites

The problem of the poor stabilities of $MAPbX_3$ and $FAPbX_3$ perovskites were faced by mixing the two cations together in the perovskite structure resulting in a mixed cation perovskite. However, the MA/FA cation structure is very sensitive to manufacture circumstances, due to the structural and thermal instability. Today the best performing (high efficiency) PSCs are fabricated from perovskite materials containing mixed cations and halides. The $MAPbI_3$-based perovskites have never achieved PCE over 20 %. [25] The HOMO and LUMO levels of $MAPbI_3$ and $(FAPbI_3)_x(MAPbBr_3)_{1-x}$ mixed cation perovskite are compared to TiO_2 and SnO_2 compact layers and they are shown in Figure 4. In the figure, we can see that the $MAPbI_3$ does not match both the LUMO levels of the presented compact layers, while the mixed cation perovskite matches well the LUMO levels of the SnO_2 compact layer. The barrier-free bandgaps are very important for charge transfer through the material interfaces in the solar cell. The band misalignment between electron transport layer (ETL) and the perovskite layer can lead to strong hysteresis behavior and scan rate dependent current densities, indicating capacitive effects at the

interface. [15]

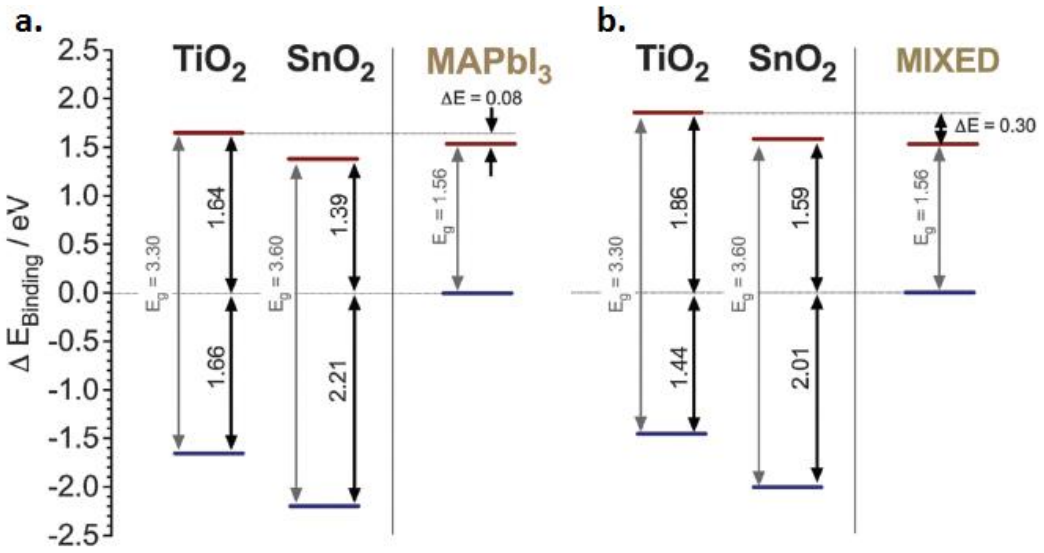

Figure 4. *The HOMO and LUMO levels of TiO_2, SnO_2, (a) $MAPbI_3$ and (b) mixed cation perovskite, $(FAPbI_3)_{0.85}(MAPbBr_3)_{0.15}$ (adapted from Ref. [15]).*

Recent research on the mixed cation perovskites have shown that a small amount of MA is already able to stabilize the crystallization of FA perovskite. MA induces a preferable crystallization into the photoactive phase of FA perovskite, and the resulting mixed cation MA/FA perovskite is both thermally and structurally more stable than either the MA or FA single cation perovskites. This finding suggests that small cations like MA play a key role in the formation of photoactive black phase FA perovskite. However, the MA/FA mixed cation perovskite still shows traces of the photoinactive yellow phase and even small quantities of the yellow phase influence the crystal growth and morphology of the perovskite. This has a negative impact on the charge collection in the cells, which limits the cell performance. [25]

Cs has also been studied in the mixed cation perovskites. When Cs replaced a small amount of the MA ions in $MAPbI_3$, a remarkable enhancement in V_{oc}, J_{sc} and PCE was achieved. The replacement of part of the MA ions with Cs optimizes the optical and electrical properties of the perovskite while maintaining the fundamental characteristics of $MAPbI_3$. Replacing 10 % of MA with Cs led to the best cell performance with PCE ~8 % via improvement in light absorption and morphology. The excess of Cs doping induces a decrease in cell performance, which can be attributed to the wider bandgap of $CsPbI_3$ compared to $MAPbI_3$ and the presence of additional crystal phases such as CsI, PbI_2 and Cs_4PbI_6. [31] Replacing 10 % of FA with Cs in $FAPbI_3$ perovskite was found to substantially improve photo- and moisture stability of the perovskite and thus enhancing the cell performance. The significant improvement with Cs/FA mixed perovskite compared to single cation FA perovskite is due to enhanced interaction between FA ion and iodide in

the crystal structure. In addition, the trap density in the perovskite lattice is reduced, leading to increase in V_{oc} and FF and thus increase in PCE up to 16.5 %. [32] The enhancement of the Cs/FA perovskite with respect to $FAPbI_3$ allows concluding that Cs is effective in guiding the crystallization towards the black phase of the perovskite. This is due to the large size different between Cs and FA. Replacing a small fraction of iodide with bromide in Cs/FA mixed cation perovskite resulting a $Cs_{0.2}FA_{0.8}PbI_{3-x}Br_x$ structure improved the PCE up to 18 % by the bandgap broadening due to increasing Br concentration. [33]

3.1.3 Triple Cation Perovskites

By adding a small amount of cesium to the MA/FA mixed cation structure a triple cation perovskite is formed. The Cs/MA/FA triple cation perovskites' crystalline structure is very organized and results into a cleaner perovskite layer. Moreover, it shows suppressed traces of yellow phase due to enhanced *t* value towards a cubic lattice structure that matches the black perovskite phase. The shift of the *t* value originates from the influence of small Cs cation on the MA/FA mixed cation. This results to a lowering of the effective Cs/MA/FA cation radius in the new perovskite material. The cleaner and well-organized crystal structure generate uniform grains, which enable better charge transport in the perovskite layer. This induces more consistent and superior cell performances and higher FFs. The triple cation structure is also more stable in ambient air and humidity and it has achieved great results even for 250 hours aging tests, extremely good for a perovskite material. [25] With a planar cell structure with SnO_2 compact layer, triple cation perovskite and $N^2,N^2,N^{2'},N^{2'},N^7,N^7,N^{7'},N^{7'}$-octakis(4-methoxyphenyl)-9,9′-spirobi[9H-fluorene]-2,2′,7,7′-tetramine (spiro-OMeTAD) hole transport material (HTM), almost 21 % efficiency has been reached. [26]

The use of all three cations, Cs, MA and FA, provides excessive versatility in fine adjustment of the perovskite film. This may also ease the negative influence of the large mismatch between the Cs and FA cations since in the mixture with MA the relative size differences of the cations are smaller. This could in turn decrease the entropic preference for phase separation in the structure. Usually the formation of the black phase perovskite requires annealing in relatively high temperatures but the addition of Cs to the perovskite structure induces the black phase in room temperature immediately after deposition. From this, it has been depicted that the Cs/MA/FA triple cation perovskite is not particularly sensitive to relatively small temperature variations during processing. [25]

With the information from the former chapters, we can conclude that a superior perovskite material for PV devices should contain multiple cations, including Cs, and mixed halides, I and Br on the X site. The best performing cells today contain Pb anion. However, due to its negative influence on the environment better options are constantly researched.

3.2 Solar Cell Structure

The main processes behind the solar cell functioning are (1) the absorption of light by the active layer and charge generation, (2) transportation of free charge carriers to their respective electrodes and (3) collection of free carriers in the electrodes and thus providing power to external circuit. [14] A typical architecture of PSC is FTO/ETL/perovskite/HTL/Au, where HTL is the hole transport layer. Fluorine–doped tin oxide (FTO) layer on the glass substrate acts as a bottom electrode. Gold is the top electrode of the cell. The absorption of light occurs in the perovskite layer located in the middle of the solar cell. The generated charges are then transported to the charge transport layers, and finally collected on the top and bottom electrodes. Besides the perovskite layer, the choice of charge transport materials has also a great influence on the cell performance. The charge transport layers can have an influence on the passivation of trap states, enhance the sustainability against moisture, template for perovskite crystallization and hinder the hysteresis effect [22, 34, 35].

3.2.1 Electron Transport Layer

The ETL delivers the photo-generated electrons from the perovskite layer to the corresponding electrode, while serving at the same time as hole blocking layer to hinder the charge recombination. Besides the electric properties of the electron transport material (ETM), the contact between ETL and electrode and the optimizing the interface between ETL and the perovskite layer play an important role in the cell performance.

The characteristics of an optimal ETL are good charge mobility, appropriate energy level alignment, minimum amount of trap states, sufficient morphology and related interfacial properties to suppress the charge recombination in the material interfaces. The morphology of the ETL has also an influence in the deposition of the perovskite layer. The electron mobility in ETL is one of the most important factors in determining devices' PV performance. As can be concluded, a high electron mobility is desired for ETL to enable efficient charge transport and collection. The bandgap of the ETL should match the bandgap of the perovskite to achieve good electron extraction and transport which in turn have a positive influence on increasing the J_{sc} and FF of the cell. The energy level adjustments of the ETL and HTL are also used to enhance the V_{oc} of the cell. [36]

Both inorganic ETMs, like TiO_2, ZnO and SnO_2, as well as organic ETMs, like fullerene and its derivatives, have been used in PSCs. TiO_2 has been the most-widely adopted ETM today but it requires high processing temperatures and shows a clear hysteresis of the IV-curve. Metal oxides have also shown performance degradation upon UV exposure. The use of fullerene derivates like PCBM ([6,6]-Phenyl C_{61} butyric acid methyl ester) as ETM with $MAPbI_3$ perovskite has improved influence on the hysteresis behavior compared to the cell with TiO_2 ETL due to improved interfacial charge transfer between the ETL and perovskite layer. Organic based ETMs exhibit also advantages in mild solution processing

and good tunability of the physical properties. SnO_2 has high transparency, high mobility and a favorable bandgap related to both $MAPbI_2$ and MA/FA the mixed cation perovskite, as seen in Figure 4. The use of SnO_2 as ETM also enables the fabrication of PSC with high efficiencies, long-term air stability, and improved hysteretic behavior at low processing temperatures (< 120 °C). The charge transport properties of inorganic ETMs can be further improved with appropriate substitution of selected additives or dopants like Nb^{5+}, Y^{3+} and Al^{3+}. Finally, an addition of a thin wide bandgap metal oxide, like MgO, Y_2O_3 or Al_2O_3, or the interfacial modification with functional self-assembled monolayer layer can enhance the cell performance. [15, 36, 37]

The variety of the deposition methods for ETL fabrication is wide. Well-known deposition methods for ETL are vapor deposition, atomic layer deposition (ALD), spin coating, spray pyrolysis, and chemical bath deposition (CBD). Spin coating is fast and easy method for thin film fabrication and the equipment is relatively cheap. CBD method does not require any specific equipment, but it can be carried out with a suitable glass container and a furnace. The samples are placed into the glass container, which is filled with the deposition solution or the bath solution. The container is then placed in the furnace where the samples absorb the compact layer on to their surface from the solution. Spray pyrolysis is a powerful technology for the fabrication of nanocrystalline thin films, and it can be used for a wide variety of materials. The method has been used for decades in solar cell production and it is very cost efficient technology. The technique does not require vacuum, provides high flexibility in terms of material composition and it is suitable for fabrication of thin films on full wafer-size. In spray pyrolysis, a liquid source is used for spraying the film on the substrate, which is heated during the deposition. The precursor solution is first atomized by pressure or air blast, and then transported to the substrate surface as droplets. On the substrate surface, the precursor solution is decomposed due to heating and initiates the film growth. [38] ALD method is excellent method for fabricating very thin and uniform films with high purity but the method requires expensive equipment.

In the experimental section, the TiO_2 and SnO_2 ETLs are fabricated with different methods in ambient air and humidity. The influence of the fabricated ETLs on the cell performance are researched with IV measurement and the qualities of the ETLs are also investigated with SEM.

3.2.2 Perovskite Layer

Perovskite forms the active, light absorbing layer in PSCs and the perovskite layer is usually several hundreds of nanometers thick. Perovskite layer is located in the solar cell between the ETL and the HTL. Charge carriers are formed when photons are absorbed in the perovskite layer, and the charge carriers transport the formed negative and positive charges to the ETL and HTL materials, respectively. [11] The charge generation and transfer in perovskite layer are explained in more detailed in chapters 2.2 and 2.3. As

stated earlier, perovskite materials have exceptional material properties resulting in high performance solar cells.

Perovskite layer is usually fabricated by solution fabrication methods, like one-step anti-solvent or two-step sequential method but also other methods like vapor deposition method are used. With vapor deposition method and planar cell architecture, PCEs over 15 % have been achieved, and the method provides good uniform perovskite films [39]. When thinking of the commercialization of the PSCs, the solution fabrication methods are though generally more attractive fabrication methods compared to vapor deposition method due to the cheaper mass production. The current challenge with solution fabrication methods is the difficulty in forming consistent and compact films. This is mainly due to the rapid crystallization of perovskite during the solvent evaporation leading to anisotropic crystals. However, by controlling the crystallization process, high quality films obtaining excellent optoelectronic properties can be achieved.

Spin coating is one of the cheapest film production methods for solution fabrication, which makes it a widely applied method. Additionally, the film fabrication by spin coating is also fast and easy. The evaporation of the solvent and self-assembly of the film during spinning induce the formation of well-crystallized perovskite film immediately. However, it is difficult to achieve a perovskite layer with uniform thickness over a large area with simple spin coating. It has been reported that the uniformity of the perovskite layer is also dependent on the thickness and homogeneity of the layer on which the perovskite is deposited (ETL in this case). This limits the applicability of the solution process. The spin coating by one-step anti-solvent method however has produced high-quality perovskite films. In the anti-solvent method, the perovskite is pipetted on to the sample and the solvent is pipetted separately on to the spinning substrate. For example in the case of $MAPbI_3$ perovskite and dimethyl sulfoxide (DMSO) as a solvent, an intermediate product, MAI-PbI_2-DMSO, is formed, which slows down the crystal growth of perovskite. One-step antisolvent method can produce shiny, smooth perovskite films with excellent electronic properties. This method has been widely used by different research groups and excellent results have been attained: a PCE close to 21 % was achieved with a planar architecture. [37, 40]

Another widely adapted solution fabrication method is two-step method, which also allows achieving films of good quality. When depositing $MAPbI_3$ perovskite by two-step method, PbI_2 is first introduced on to the substrate by spin coating, followed by exposing to MAI solution. In this step, PbI_2 and MAI react producing the $MAPbI_3$ perovskite layer. The resulting perovskite film obtained a PCE of 15 % with mesoscopic device. Recently, the method has been combined with PMMA crystal growth templating, producing films with suppressed amount of defects and larger well-oriented grains. This resulted in certified PCE of 21.02 %. [41, 42]

In this work, the fabrication of $MAPbI_3$ and Cs/MA/FA perovskites are performed in ambient air with humidity of ~45 % rH. The influence of fabrication circumstances is studied by IV measurements, by comparing the experimental results with the reference data from the literature for the corresponding materials, and with those of devices were fabricated in glove box at University of Cologne. The final goal is to demonstrate the necessity of the inert fabrication circumstances for the perovskite and for the overall device fabrication.

3.2.3 Hole Transport Layer

HTL is deposited in the solar cell between perovskite layer and electrode and its function is to transfer the positive charges generated in the perovskite layer to the electrode. As in the case of ETL, also HTL has an influence on the cell performance and it should have ideal charge transport properties and matching bandgap with the perovskite material. Most commonly used HTM today is spiro-OMeTAD, whose molecular structure is presented in Figure 5. Spiro-OMeTAD is usually fabricated by spin coating on top of the perovskite layer.

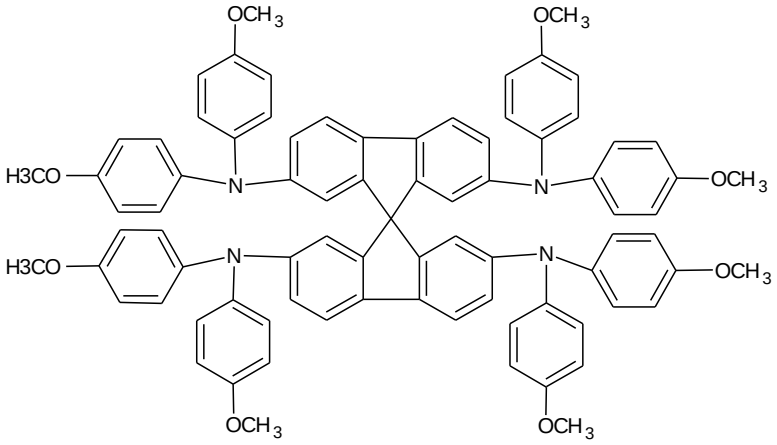

Figure 5. *The molecular structure of spiro-OMeTAD.*

Spiro-OMeTAD requires additive doping for to sufficient charge transport due to its low conductivity. Typical additives used for doping of spiro-OMeTAD are bis(trifluoromethylsulfonyl)imide salt (LiTFSI), tris(bis(trifluoromethylsulfonyl)imide) (FK209) and 4-tertbutyl pyridine (TBP). This results in complicated device fabrication and weakened device stability. Spiro-OMeTAD is also very expensive, since its synthesis is difficult. This has a remarkable impact on the overall cost of PSCs. Hence, cheaper, easily fabricated and dopant-free HTMs are constantly researched. [43]

Under illumination, spiro-OMeTAD oxidizes towards the radical cation spiro-$OMeTAD^+$ resulting in decrease in the absorption band. The oxidation of spiro-OMeTAD is exclusively a photo-induced phenomenon and it is accelerated by the presence of oxygen or additives. From this we can conclude that the inert working conditions will not eliminate

the problem with the oxidation of the spiro-OMeTAD layer during fabrication. The solar cells including spiro-OMeTAD HTM suffer from this photo-induced evolution, since the solar cell working conditions require relatively strong illumination. [43] Thus, the oxidation of spiro-OMeTAD has direct consequences not only on device performance but also on the device stability. The photovoltaic performance of spiro-OMeTAD has been improved with pyridine additives, which on the other hand corrode the perovskite by forming complexes with PbI_2. [44]

3.3 Solar Cell Architectures

Two of the most common perovskite solar cell architectures are mesoscopic and planar cell structures. Perovskite solar cell can also be adopted in 'perovskite sensitized solar cell' (PSSC) configurations, where a similar concept as in dye sensitized solar cells (DSSC) is used, with perovskite being the sensitizer. Additionally few other cell architectures for perovskite solar cells are known but they are rarely adopted. [19, p. 249] By means of both planar and mesoscopic PSCs it has been possible to achieve high efficiency cells, with PCE over 20 %, and the superiority of either of the architectures is currently unestablished.

Perovskite was used in solar cells for the first time in PSSCs in 2009. The first PSSCs were made of a $MAPbI_3$ perovskite layer and liquid electrolyte containing iodide-tri-iodide redox couples. The PCE of those cells was 3.5 % [29]. One of the PSSCs major weaknesses was the use of liquid electrolyte, which made the devices very unstable. In fact, in the liquid electrolyte perovskite dissolves and dissociates in minutes. This is also the reason why it has not been possible to obtain highly efficient PSSCs. Later PSSCs achieved 6.5 % efficiency by optimizing the structure of the electrolyte and enhancing the fabrication of the perovskite layer [29]. The more efficient PSSCs were made of mesoporous TiO_2 layer that was sensitized with $MAPbI_3$ nanoparticles, and deposited on a dense TiO_2 ETL. Spiro-OMeTAD was used as a solid HTM. The use of solid HTM instead of liquid electrolyte improved the extremely low stability of PSCs. The solid HTM also improved the cell performance due to the more efficient light absorption compared to liquid electrolyte. Spiro-OMeTAD as s solid HTM could achieve a complete absorption with 500 nm film thickness but instead for the liquid electrolytes the necessary film thickness is approximately 2 μm. The HTM infiltration was important to induce a contact between HTL and perovskite sensitized ETL. The purpose of the mesoporous oxide layer in PSSCs is to receive and separate the excited electrons, while that of the dense TiO_2 is to prevent direct contact between transparent, conducting oxide layer on top of the glass substrate and HTM as described in chapter 3.2.1. With PSSCs consisted of $MAPbI_3$ perovskite and TiO_2 ETL and solid HTL a PCE of 9.7 % was achieved. [19, pp. 249−250, 29, 45] These solid state perovskite cells have been fabricated and developed since 2012.

Lately, the sensitized TiO_2 had also been replaced by mesoporous Al_2O_3 with remarkably faster electron diffusion through the perovskite layer. This delivered a V_{oc} over 1.1 V. It was noticed that Al_2O_3 did not work as an electron injecting structure but rather as a scaffold layer for perovskite. [2, 46] This is where the research of non-sensitized perovskite solar cells begun. In the experimental part of the work, both the mesoscopic and planar devices are fabricated with different ETLs and perovskite materials in ambient conditions.

3.3.1 Mesoscopic Cells

In mesoscopic PSC, the perovskite layer is deposited on top of the mesoporous scaffold layer (like Al_2O_3 or TiO_2). The charge transfer from perovskite layer to spiro-OMeTAD is efficient, and it induces long-lasting charges in the perovskite layer. In the case of mesostructured cells, the uniform perovskite layer on top of mesoporous scaffold layer is very important and the charge transport from perovskite to ETL is not possible if the perovskite layer is not uniform. [2, 19, p. 249] The first mesoscopic cells achieved 10.9 % PCE [45]. A mesoscopic PSC with an architecture of FTO/bl-TiO_2/mp-TiO_2/perovskite/spiro-OMeTAD/Au is presented in Figure 6. In the figure, 'bl' stands for blocking layer since compact ETL acts as a blocking barrier for holes, and 'mp' means mesoporous layer. By optimizing the manufacturing methods and changing the mesoporous TiO_2 to Al_2O_3, efficiencies as high as 15 % were achieved [29].

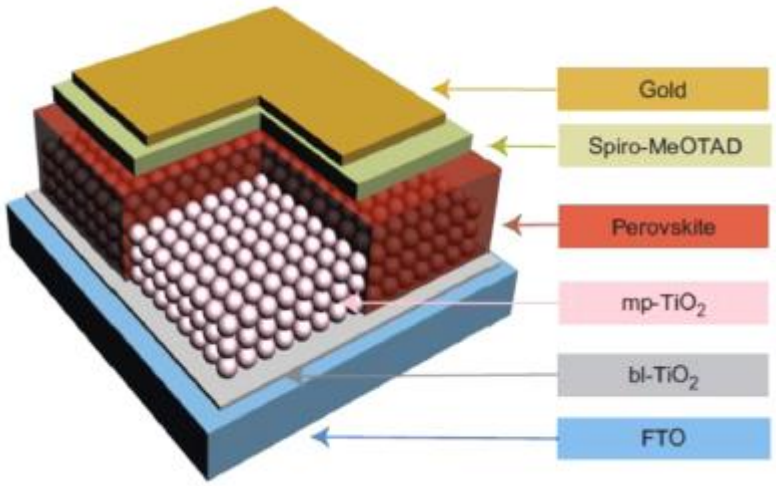

Figure 6. *The cross section image of mesoporous perovskite solar cells. The layers are from top to bottom the top electrode (Au), HTL (*spiro-OMeTAD*), perovskite layer, mesoporous (mp-TiO_2) and hole blocking compact ETLs (bl-TiO_2) and the oxidized glass substrate (FTO) as a bottom electrode (adapted from Ref. [17] with permission of Elsevier, Copyright 2016). Spiro-OMeTAD can be written also as spiro-MeOTAD depending on the reference, but both styles are considered as correct.*

The role of mesoporous TiO_2 layer in the cell structure has not been clearly solved but it has been argued whether the electrons are injected into mesoporous TiO_2 to be collected through it. However, the mesoporous TiO_2 is assumed to be an extension of the compact TiO_2 layer, and it operates as an effective heterojunction capable of suppressing charge recombination dynamics. [47] The pore size of the mesoporous scaffold restricts the perovskite grain size resulting in smaller perovskite crystals compared to the planar device structure. Recent studies have shown a correlation between perovskite crystal size and charge transport rates. The smaller grain size in mesoscopic devices is likely to induce charge scattering or trapping at the numerous grain boundaries. The slower charge transfer rates may also be related to the insulating of mesoporous layer nanoparticles, hindering the charge movement inside the perovskite layer. Additionally, insufficient pore-filling of perovskite within the mesoporous scaffold is likely to hinder the charge diffusion. However, the electron injection rates into a mesoporous TiO_2 scaffold have proven to be significantly faster than to the compact TiO_2 layer and the mesoporous scaffold layer is capable of reducing the charge recombination across the FTO, compact TiO_2 layer, and perovskite interfaces. [48]

Mesoscopic PSCs can achieve high efficiencies at relatively low mesoporous TiO_2 thicknesses. While the typical thickness of the mesoporous layer is 10–15 μm in PSSCs and ~3 μm in solid state PSSCs, for mesoscopic PSCs the thickness of mesoporous layer can be as low as 350 nm. This implicates that the smaller thickness of the mesoporous layer is better when considering the cell performance. The high efficiencies with low mesoporous layer thickness are due to the high optical absorption coefficient of $MAPbI_3$. Nevertheless, the exact dependence is determined by the perovskite distribution within the TiO_2 layers and the thickness of the perovskite layer. Recent studies have also shown that PSCs with mesoporous TiO_2 layer can also function without HTL. These type of cells are called HTL-free perovskite cells. [20]

3.3.2 Planar Cells

In planar PSCs, the mesoporous scaffold layer is absent, due to organic lead halide perovskites ability to transfer electrons and holes by themselves, thanks to their long lifetimes of the charges and long diffusion lengths. This enables the perovskite layer to be deposited directly between two selective charge transport layers in planar PSCs. Normally the ETL is below the perovskite layer and the HTL is on top of the perovskite layer but the structure can also be inverted planar where the HTL and ETL are on the opposite sides with respect to the perovskite layer. In planar PSCs, a dense and smooth perovskite layer is important in order to prevent the collision of the charge transport paths to each other's, and to gain good contacts on the layer interfaces. [2, 19, pp. 249−254] The structure of planar PSC is exactly the same kind as presented in Figure 6 except without the mesoporous TiO_2 layer. The discovery of the planar cell architecture for PSCs proved that the

charge separation can occur in the perovskite absorber and that the efficient charge diffusion occurs for both electrons and holes [21, 45].

Large perovskite crystals are typical for planar cell structures since the crystallization is usually fast and there are no mesoporous scaffold layer restricting the grain growth. The large perovskite grains exhibit longer radiative charge recombination lifetimes and faster charge transfer compared to the perovskite with smaller grain size in mesoscopic cells. These features show an inherent advantage of perovskite morphologies over mesoscopic morphologies. On the other hand, there is a limited contact between the compact ETL and the perovskite layer in planar structure, which hinders the extraction of electrons from perovskite to ETL. However, in mesoscopic cell structures, this is not the case and electron injection to mesoporous layer is significantly faster. [48]

The advantage of planar cell fabrication over the mesoscopic cell fabrication is that it does not require the deposition of complex nanostructure between ETL and perovskite layer leading to a simplified device architecture. However, fabrication of thin and pinhole free layers by solution processed methods is difficult. The mesoporous layer on top of compact ETL can cover the pinholes in the compact layer and by so prevent the contact between the perovskite layer and electrode. Poor film coverage results in poor light absorption and shunt paths through the perovskite layer, thus reducing the cell efficiency [20].

3.4 Stability Issues

In order to commercialize the perovskite solar cells achieving high efficiencies is not enough. The cells need to be also stabile, long lasting, resistant to heat and humidity and they should not release toxic materials to the environment. These are all current issues with perovskite solar cells and they are all under an intense research.

3.4.1 Device Stability

The stability of the PCSs was at its poorest before the discovery of the solid HTM and the cell efficiency and stability of the cells increased remarkably after the discovery of spiro-OMeTAD. However, the solid HTMs are still one of the most important research subjects in perovskite solar cell research since spiro-OMeTAD is very expensive and difficult to synthesize as mentioned earlier. [2]

The most efficient PSCs include hybrid lead halide materials with great absorption coefficient but weak stability. The cells are typically manufactured in controlled environment, i.e. in nitrogen glove box in the absence of oxygen and humidity. When the cells are brought to ambient air, the perovskite starts to decompose fast because of the humidity, oxygen, light, and heat. The charge transfer layers can also degrade in the cells due to the same factors. [45, 46] Perovskite can also react with the top or bottom electrodes if they

come in contact with each other, e.g. due to pinholes in the charge transport layers or humidity, which would also weaken the cell stability.

If the metal electrode evaporates from the HTL surface it can diffuse into the HTL even 10 nm deep. This can allow a contact between the electrode and the perovskite layer. This is possible for example if the HTL is too thin and it would cause a severe damage for the metal electrode. If the HTL is very thick, it could isolate the metal electrode from the perovskite layer but also weaken the charge mobilities and lower the cell efficiency. Compared to the organic charge transfer materials, metal oxide nanoparticles as HTMs like NiO_x have showed a good improvement to this issue. Metal oxide materials are usually stabile in ambient air, dense enough to isolate the perovskite from the electrode and to protect the perovskite from humidity. Metal oxides also have good charge mobilities and they are easy to manufacture at low temperatures. However, the cells with metal oxide HTMs have not yet succeeded in achieving as high efficiencies as the cells which contain spiro-OMeTAD as HTM. [46]

The metal oxide ETL material affects the stability of the perovskite solar cell and the manufacturing costs. Commonly used transition metal oxides as ETMs are ZnO, TiO_2 and SnO_2. Among these three metal oxides, ZnO and SnO_2 can be deposited by low-temperature processes and their electron mobilitites are much higher than in TiO_2. Fabrication of TiO_2 also requires temperatures as high as 450 °C. However, when lead halide perovskite is deposited on ZnO the perovskite layer becomes thermally unstable and it suffers from fast perovskite degradation as the temperature rises up to 80 °C. SnO_2 has the same advantages over TiO_2 including good stability, high optical transparency and barrier-free energetic configuration. Above all, the SnO_2 layer could be grown on top of the thin-film solar cell to protect the perovskite against moisture. [49]

The biggest threats for the stability of PSCs arising from the surroundings are humidity, heat, light and oxygen, which lower the cell efficiency by perovskite degradation. In the case of $MAPbI_3$ the possible decomposition mechanism in moisture is presented in equations 13-16 and the mechanism is shown to accelerate by heat. At first $MAPbI_3$ is decomposed to solid PbI_2 and aqueous MAI (13), which is further decomposed into CH_3NH_2 and HI (14). HI will further decompose to solid iodine, liquid water and gaseous hydrogen due to oxygen (15) and illumination (16). [50]

$$CH_3NH_3PbI_3\ (s) \rightleftharpoons PbI_2\ (s) + CH_3NH_3I\ (aq) \qquad (13)$$

$$CH_3NH_3I\ (aq) \rightleftharpoons CH_3NH_2\ (aq) + HI\ (aq) \qquad (14)$$

$$4\ HI\ (aq) + O_2\ (g) \rightleftharpoons 2\ I_2\ (s) + 2\ H_2O\ (l) \qquad (15)$$

$$2\ HI\ (aq) \rightleftharpoons H_2\ (g) + I_2\ (s) \qquad (16)$$

At temperatures higher than 150 °C, $MAPbI_3$ decomposes into its components CH_3NH_2, PbI_2 and HI. The reaction mechanism is presented in equation 17 and it is the reverse reaction for $MAPbI_3$ formation. [50]

$$CH_3NH_3PbI_3\ (s) \rightleftharpoons PbI_2\ (s) + CH_3NH_3I\ (aq) + H_2\ (g) \qquad (17)$$

The current class of hybrid perovskites is also sensitive to illumination, and they decompose in light. The possible mechanism for the $MAPbI_3$ decomposition when exposed to light is presented in equations 17-20. At first $MAPbI_3$ is decomposed into its components as in presented in the equation 17. At the interface between ETL and $MAPbI_3$ the ETM can extract electron from I^- by oxidizing it to solid iodine and affecting the deconstruction of the crystal structure of $MAPbI_3$ (18). At the same time, MA^+ ion loses a proton and CH_3NH_2 gas is formed (19). Finally, iodine acquires the electrons and reacts with protons forming gaseous HI (20). [50]

$$2\ I^-\ (aq) \rightleftharpoons I_2\ (s) + 2\ e^- \qquad (18)$$

$$3\ CH_3NH_3^+\ (aq) \rightleftharpoons 3\ CH_3NH_2\ (g) + 3\ H^+\ (aq) \qquad (19)$$

$$I^-\ (aq) + I_2\ (s) + 3\ H^+\ (aq) + 2\ e^- \rightleftharpoons 3\ HI\ (aq) \qquad (20)$$

The previous reactions also release toxic PbI_2 to environment, which is a highly unfavorable side effect for the perovskite decomposition. To avoid the perovskite degradation, a several protecting methods with interfacial layers have been researched. Nevertheless, the focus of the stability improvement has been concentrated on the modification of perovskites themselves. A small lattice expansion or distortion can cause a symmetry change to the perovskite structure, which could give structural stability to the material. [50] As denoted in the chapter 3.1, $MAPbI_3$ perovskite can be stabilized with cation substitution and even more with Cs/MA/FA triple cation perovskite that has showed a remarkable improvement in perovskite stability and achieved a stable PCE of 21.1 %. The anion substitution also discussed in chapter 3.1 allowed improving the perovskite stability. In the experimental section of this work, the influence of ambient air and humidity are researched on the fabrication of $MAPbI_3$ and Cs/MA/FA triple cation PSCs, and the device stabilities are presented with ageing measurement results. The target is to find out if the outstanding device stability of triple cation PSC is maintained when the device is fabricated in the presence of ambient air and humidity.

3.4.2 Hysteresis Effect

Hysteresis effect is an abnormal behavior seen in the device IV measurements, and it is one of the most challenging issues with PSCs to date. Hysteresis behavior makes the actual device efficiency determination difficult since the efficiency obtained from the reverse scan is inconsistent with forward scan and thus different scan rates result to different

characterization. It has also been noticed that higher scan rates result in increased efficiency. Additionally, the scan history of the device and light exposure have influence on the hysteresis. The result of the hysteresis effect is shown in Figure 7 for both planar and mesoscopic device structures based on $MAPbI_3$ and TiO_2. As it can be seen in the figure, the hysteresis effect is strongly dependent on the device structure and it is much stronger for planar device when compared to the mesoscopic device. Actually, the hysteresis is relatively weak for the mesoscopic device due to the use of mesoporous TiO_2 layer. The mesoporous layer increases the contact area between the perovskite layer and TiO_2, which improves the charge transfer from perovskite to TiO_2. In addition, the small perovskite grains in the TiO_2 pores might influence the decrease in hysteresis. [51]

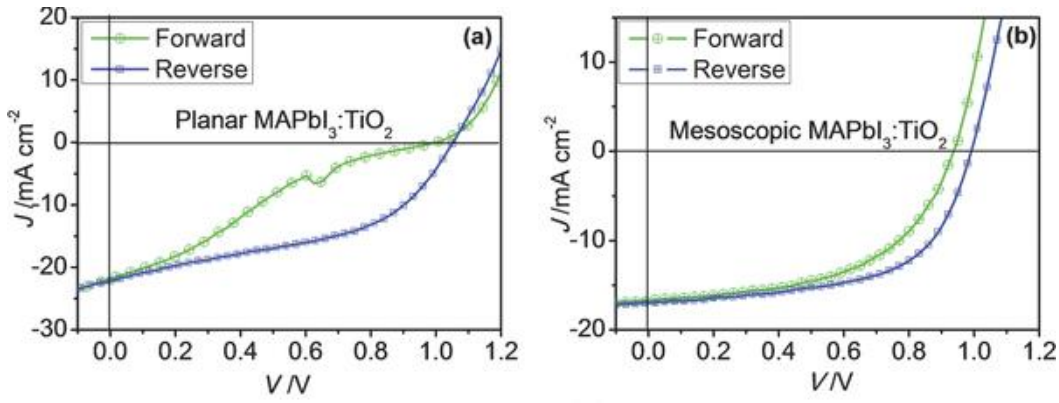

Figure 7. *Typical hysteresis effect present in planar (left) $MAPbI_3/TiO_2$ and mesoscopic (right) $MAPbI_3/TiO_2$ PSCs (adapted from Ref. [51] with permission of John Wiley and Sons, Copyright 2015). The vertical axis shows the J_{sc} and horizontal axis is the scan voltage, V. Both devices have been measured with a scan rate of 1 V/s.*

The origins of the hysteresis effect remains ambiguous, but several suggestions exist based on recent research. Proposed origins include slow trapping and detrapping of charge carries due to the subgap traps of solution processed perovskite, changes to the ferroelectric structure of the device, and ion migration. [51] It was noted that the hysteresis effect in the cells containing TiO_2 relates to the deep charge traps in TiO_2 layer, which are affected by the low electron mobilities, induced charge accumulation, and UV light induced oxygen vacancies. As an answer to this problem, organic ETLs have been adopted as ETMs but they show lower efficiencies compared to the devices employing TiO_2 ETL. As mentioned in chapter 3.2.1, fullerene derivatives as ETM have been successful in reducing the hysteresis effect since their ability to reduce the density of the trap states and passivate the grain boundaries of perovskite layer. The PSCs with fullerene ETL have achieved a hysteresis free devices with PCE up to 19.1 %. The top efficiency cells have though demanded a vacuum processed ETL and the IV measurement have been performed in inert environment in glove box. [52] Vacuum processing of ETL is more complicated, slower, and more expensive compared to solution processing methods and measuring the IV curves in inert environment is far from the circumstance of the working conditions of the solar cells.

Replacing TiO_2 ETL with SnO_2 has an influence on the decrease of hysteresis effect, though the hysteresis with SnO_2 ETL varies substantially for the different deposition methods [37]. In the experimental section, the IV curves for different device structures with both TiO_2 and SnO_2 ETLs are fabricated. The influence of ambient working conditions on the hysteresis effect in each case is studied and reported.

4. MATERIALS AND METHODS

The samples were fabricated in ISO 6 clean room at TUT in ambient air. During the fabrication process the ambient temperature and humidity was ~21 °C and ~45 % rH. The samples were fabricated on TEC 7 Pilkington FTO plates, cut to an approximate size of 2 x 2 cm. The $CH_3NH_2 \cdot HI$, $PbBr_2$ and PbI_2 were purchased from TCI Chemicals, TiO_2 30 NR-D and 18 NR-T pastes, $CH(NH_2)_2I$, and CH_3NH_3Br from Dyesol, CsI from abcr GmbH, spiro-OMeTAD from Lumtec and FK209 from Dyenamo. All the other chemicals used were purchased from Sigma-Aldrich. The samples were stored in desiccator cabinet in 10 % rH between the fabrication steps.

4.1 Solar Cell Fabrication

The FTO plates were etched either chemically or mechanically. Chemical etching was done by protecting the etched area with Kapton tape, and oxidizing the FTO layer with zinc powder and 4 M HCl. Mechanical etching was performed with a grinding tool (Dremel). After etching, the plates were cleaned carefully to prevent any impurities on FTO surface. The plates were first cleaned with Hellmanex 2 % solution and toothbrush, treated with ultrasonic bath in Hellmanex 2 % for 15 minutes and washed with abundant MilliQ water and ethanol. Then an ultrasonic bath with isopropanol for 15 minutes was obtained, and finally the plates were heated on a hot plate at 150 °C for no less than 30 minutes. If the fabrication process was not carried out the next day at the latest a retreatment with ultrasonic bath in isopropanol and heating at 150 °C was required.

4.1.1 Compact and Mesoporous Layers

Two different compact layer materials were applied (TiO_2 and SnO_2), and two different fabrication methods for TiO_2 compact layer and three for SnO_2 compact layer were experimented. Before the compact layer deposition, the plates were protected with Kapton tape and treated with ultraviolet-ozone surface treatment, UVO for 10 and 15 minutes for TiO_2 and SnO_2 samples, respectively, right before the compact layer deposition.

SnO_2 compact layer was prepared by spin coating, chemical bath deposition, CBD or by applying both of these methods. SnO_2 by spin coating was carried out by first preparing the solution for the layer fabrication. A 0.05 M $SnCl_4 \cdot 5\ H_2O$ in isopropyl alcohol was prepared and put to a magnetic stirrer for 30 minutes. The spin coating was performed by depositing 70 µl of the 0.05 M $SnCl_4 \cdot 5\ H_2O$ in isopropyl alcohol with spin program 3000 rpm and 200 rpm/s for 30 seconds. After the spin coating a pre-drying at 100 °C for 10 minutes was followed and then heat-treated at 180 °C on a hot plate for 1 hour. [37] The SnO_2 fabrication by spin coating is presented in Figure 8a.

SnO_2 layers by CBD were grown on FTO plates either on already spin coated samples as a post-treatment to achieve a thicker and solid compact layer. The bath solution was prepared by dissolving 2.0 g of urea in 80 ml of MilliQ water. Then 40 µl of mercaptoacetic acid, 2.0 ml of 37 wt-% HCl and $SnCl_2 \cdot 2\ H_2O$ at 0.012 M was added to the solution. The solution was put to the magnetic stirrer for 2 minutes. The samples were deposited vertically on the glass container presented in the Figure 8b and the container was filled with the bath solution. The container was placed in the furnace at 70 °C for 3 hours, treated with ultrasonic bath in MilliQ for 2 minutes to rinse the bath solution off the samples, dried with air stream and finally annealed at 180 °C on a hot plate for 1 hour. [37]

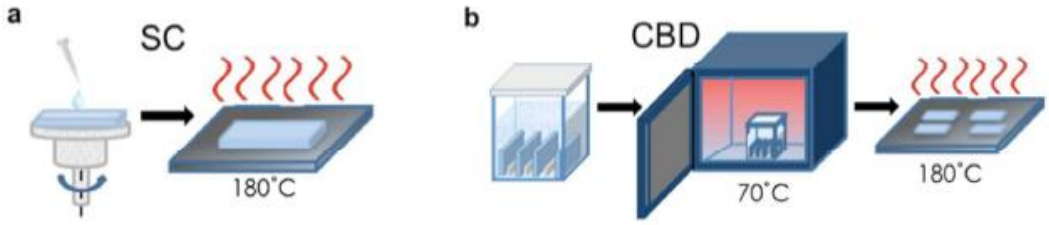

Figure 8. *Fabricating the compact SnO_2 layer by (a) spin coating and (b) chemical bath deposition (adapted from Ref. [37] with permission of Royal Society of Chemistry, Copyright 2016).*

TiO_2 compact layer was deposited on the FTO plates by spin coating or by spray pyrolysis. The spin coated layers were self-fabricated at TUT as in [53], but the spray pyrolyzed compact layers were fabricated in the AK Mathur group during Dr. Vivo's research visit at the University of Cologne.

The solution for TiO_2 compact layer fabrication, Ti-isopropoxide in absolute ethanol was prepared no earlier than 1 day before the deposition. First two precursor solutions were prepared. Precursor solution 1 was made by mixing 1.25 ml of absolute ethanol with 175 µl of titanium isopropoxide and precursor 2 by mixing 1.25 ml of absolute ethanol with 17.5 µl of 2 M HCl. The precursor solution 2 was put to the magnetic stirring while the precursor 1 was carefully dropwise added to the precursor 2. The final solution was let to mix under magnetic stirrer for no less than 30 minutes and the solution was taken to the fridge until used. The solution was taken to the room temperature and placed to the magnetic stirrer for at least 30 minutes before use on the day the solution was needed. 70 µl of Ti-isopropoxide in absolute ethanol was deposited on the FTO plate and the spin program was started. The spin coating parameters for TiO_2 compact layer are 3000 rpm, 3000 rpm/s and 30 seconds. After spin coating the samples were dried on a hot plate at 120 °C for 10 minutes. If the deposition of compact layer is followed by the deposition on mesoporous TiO_2 layer, the fabrication was continued immediately. If the fabricated cells were planar, the Kapton tapes were removed, and sintering was started according to the Table 3. The samples were let to cool down before the deposition of perovskite layer.

Table 3. *The sintering program for TiO_2 compact and mesoporous layers. Ramp is the estimated time before the targeted temperature is achieved, ramp rate is the rate for the temperature change, T is the target temperature for each ramp step and hold is the time how long each step temperature is maintained after the target temperature is reached.*

Ramp [min]	5	15	5	5	100
Ramp rate [K/min]	25	13	10	15	15
***T* [°C]**	125	325	375	450	150
Hold [min]	5	5	5	30	-

The mesoporous layer was deposited on top of the compact layer by spin coating. Before spin coating, the samples were treated with UVO for 10 minutes. Two different solutions for mesoporous layer fabrication were used with 30 NR-D or 18 NR-T titania paste. 30 NR-D and 18 NR-T transparent titania pastes contain titania nanoparticles, with average size of 30 nm (30 NR-D) or 20 nm (18 NR-T) with organic binders. The pastes have been formulated to provide versatile porosity suitable for electrolyte systems. [54] First solution option, solution 1, was prepared by measuring 0.3 g of 30 NR-D paste and dissolving it to absolute ethanol under stirring. The second option, solution 2, was prepared by measuring 18 NR-T paste and absolute ethanol 1:4 in weight and placed to a magnetic stirrer. Both of the mesoporous paste solutions need to be prepared no less than 1 day before used. The solutions are kept under stirring as long as the solutions are needed. However, the solutions should not be used approximately 1 after prepared. 50 µl of the mesoporous solution was deposited on the sample and the spin program was started. The spin coater parameters for solution 1 (30 NR-D paste) are 4000 rpm, 2000 rpm/s and 10 seconds and for solution 2 (18 NR-T paste) 5000 rpm, 2000 rpm/s and 40 seconds. After spin coating the samples were placed on a hot plate at 120 °C until all samples are spin coated. Then the Kapton tapes were removed and the sintering was started according to the Table 3.

4.1.2 Perovskite Layer

Three different recipes or methods were included with the fabrication of the perovskite layer in the solar cells. The $MAPbI_3$ perovskite layer was fabricated by two different methods, 2-step sequential and 1-step antisolvent deposition methods. The triple cation, Cs/MA/FA, perovskite was fabricated by 1-step antisolvent method only and with one main recipe which was slightly optimized during experiments. The active areas of the samples were limited with Kapton tape and the samples were treated with UVO for 15 minutes immediately before the perovskite layer deposition. After the annealing of each perovskite layer, the samples were cooled in a desiccator cabinet for 20 minutes before the HTL deposition.

The $MAPbI_3$ fabrication by 2-step sequential deposition method consists of two steps, namely the deposition of PbI_2 film and the reaction of PbI_2 and MAI. For the PbI_2 film

fabrication, 1 M PbI_2 in anhydrous DMF was prepared and heated at 100 °C under stirring until all the PbI_2 was dissolved. The solution was heated during the spin coating of all samples to avoid the PbI_2 crystallization in the solution. 60 µl of the PbI_2 solution was deposited on the sample and the spin program was started. The parameters for the spin coating are 6100 rpm, 6000 rpm/s and 30 seconds. The samples were dried on a hot plate at 70 °C for 15 minutes after spin coating and the Kapton tapes were removed. 10 mg/ml MAI in anhydrous isopropanol was prepared during the PbI_2 films were dried on a hot plate. The solution was placed into a closed vial to avoid moisture in the solution, and put to a magnetic stirrer until use. MAI is very sensitive to moisture and the solution should not be prepared in advance. The solution was poured into a dipping container, and the samples with PbI_2 film were dipped vertically to the solution for 20 seconds one at a time. The dipping solution was changed to a new one after 4 samples to avoid impurities and to maintain the approximate level of MAI in the solution. Immediately after dipping, the samples were rinsed with anhydrous propanol to wash away the unreacted MAI, though excessive soaking of the samples should be avoided. The samples were dried in spin coater with PbI_2 spin program, and annealed at 100 °C in vacuum for 30 minutes.

1-step antisolvent method differs quite much from the 2-step sequential method. In 1-step antisolvent method, the perovskite solution was deposited on the sample by spin coating and the solution was deposited separately on the sample during the sample was spinning. The 1-step antisolvent deposition of $MAPbI_3$ perovskite was made by first preparing a 2.5 M MAI stock solution in anhydrous DMSO. The perovskite solution was prepared by mixing PbI_2 and 2.5 M MAI stock solution in 1:1 ratio, and adding anhydrous DMFO to the desired volume of the solution. The perovskite solution was heated on a hot plate at 100 °C for few minutes to dissolve the PbI_2. The perovskite was deposited on the samples with a two-step spinning program. First 35 µl of perovskite solution were spread on the sample and the spin program was started. The spin coating parameters for the first step are 1000 rpm, 200 rpm/s and 10 seconds, while for the second step 6000 rpm, 2000 rpm/s and 30 seconds. 15 seconds before the end of the second spin program 100 µl of anhydrous chlorobenzene or anhydrous toluene was pipetted on to the spinning substrate. The anhydrous toluene is the antisolvent which induces the rapid perovskite crystallization immediately when deposited. After spin coating, the Kapton tapes are removed and the samples are placed on a hot plate at 100 °C for 30 minutes.

The triple cation Cs/MA/FA perovskite fabrication by 1-step antisolvent method was began with the precursor solution preparation. Precursor solution contains 1.1 M FAI, 1.2 M PbI_2, 0.2 M MABr, 0.22 M $PbBr_2$ and 0.05 M CsI in anhydrous DMF:DMSO 4:1 ratio in volume. By the end of the experiments, the concentrations of $PbBr_2$ and CsI were slightly modified to 0.2 M and 0.8 M to optimize the precursor solution. All the solid substrates were measured carefully in the same vial and the anhydrous DMF:DMSO 4:1 was prepared separately and added to the vial. The solution was mixed with Vortex for few seconds and put to a magnetic stirrer for 30 minutes. The precursor solution was

filtered with 0.2 μm filter before use and spin coated on the samples in a two steps program the same as $MAPbI_3$. After the spin coating, the samples were placed on a hot plate at 100 °C until all samples were spin coated. The Kapton tapes were removed and the samples were annealed at 100 °C either in vacuum or in air for 1 hour.

4.1.3 Hole Transport Layer and Gold Evaporation

Spiro-OMeTAD was used as HTM in all samples. 70 mM spiro-OMeTAD in anhydrous chlorobenzene was prepared by mixing the solution with, TBP, 1.8 M LiTFSI in acetonitrile, and 0.25 M FK209 in acetonitrile stock solutions. The molar ratio of additives for spiro-OMeTAD was 3.3, 0.5, and 0.05 for TBP, Li-TFSI, and FK209 respectively and the dopants were added in this order to the spiro-OMeTAD solution. The solution was kept under magnetic stirring until used. 50 μl of spiro-OMeTAD solution was deposited on the sample and the spin program was started with the following parameters: 4000 rpm, 2000 rpm/s and 20 seconds.

Before evaporating the top contact, FTO contacts were cleaned with anhydrous chlorobenzene and the evaporation masks were obtained. 80 nm thick gold layer was thermally evaporated with Edwards FL 400 evaporator at a pressure below $1*10^{-5}$ mbar. The evaporation was performed with the following evaporation rates: 0.005 nm/s up to 5 nm, 0.01 nm up to 10 nm, 0.03 nm/s up to 30 nm and 0.08 nm/s up to 80 nm. After the evaporation, the contact areas were painted with silver paint to enhance the proper contact between the gold contacts and the alligator clips during the IV-measurements.

4.2 Solar Cell Characterization

The cell performance was characterized by measuring the IV-curves for the cells. From the IV measurement, the following data was analyzed: PCE, FF, J_{sc} and V_{oc}. The cell structure was characterized by scanning electron microscope (SEM).

4.2.1 Current-Voltage Measurement

The IV curves were measured on the same or the next day after the gold was evaporated on top of the cells. The measurement was performed with a Sciencetech-SS150 AAA solar simulator equipped with a filtered 1000 W Xenon lamp to provide solar simulated irradiation under the light intensity of AM 1.5 G and 1000 W/m^2. The light source was calibrated with a reference silicon cell (Oriel Instruments). IV measurement data were recorded with Agilent E5272A source meter. Before the measurement, the cells were masked with a black cardboard specifically cut for masking one contact at a time. The area of the mask was a slightly bigger than the contact area and the active area for each contact was measured with Dino-Lite AM4113ZTL microscope after the IV measurement. The purpose of the masking is to avoid incorrect under- or over estimations during

the IV characterization. The solar simulator and the measurement set up is presented in Figure 9.

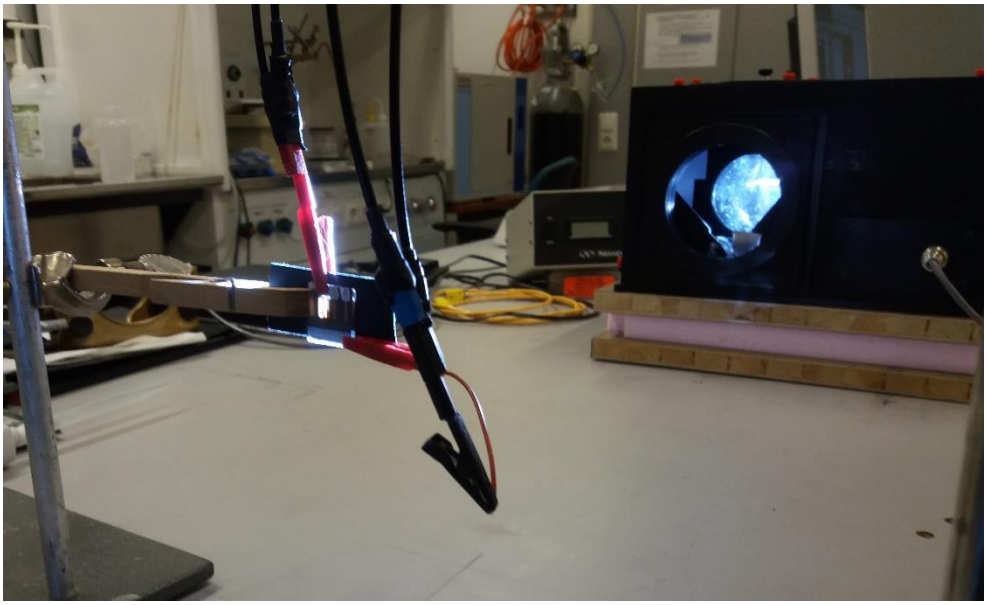

Figure 9. *The solar simulator and the measurement set up for IV measurement.*

In the figure, the solar cell is deposited to the position where the illumination is determined to be 1000 W/m^2 by the reference cell calibration. The cell is set to the position with a wooden clip, and two alligator clips are attached to the contact areas of the cell in order to get the current data to the source meter. The cells were first measured in dark with forward scan and after that with the forward scan under illumination and finally with the reverse scan under illumination. The scan rate applied was 40.5 mV/s. When choosing the scan rate, an attention was paid to avoid overestimations according to reference [55].

4.2.2 Scanning Electron Microscopy

The quality and thickness of the fabricated compact layers and final device architectures were investigated by SEM imaging. SEM is an effective equipment for observation and characterization of both organic and inorganic materials on a nanometer to micrometer scale. With SEM it is possible to obtain three-dimensional-like images of the material surfaces.

In SEM measurement, the researched area of the specific material is irradiated with a finely focused electron beam. The image is formed by swiping the electron beam in a raster across the surface. The interaction of the electron beam with the analyzed surface produces different types of signals like secondary electrons, backscattered electrons, characteristic x-rays besides other photons of various energies. The observed signals are then obtained from specific emission volumes within the sample and used for examining for

example surface topography, crystallography and composition of different layers of the sample. [56, pp. 1−2]

5. RESULTS AND DISCUSSION

The fabricated cells were characterized by IV measurements, and the IV data were analyzed for each cell in order to determine the photovoltaic parameters. Finally, the results of devices fabricated by different methods and materials were compared with each other and with the reference data from the literature. The cross sections of both planar and mesoscopic cell structures were analyzed with SEM measurements, as well as the quality of different ETLs. As a key result, the influence of ambient working conditions on the cell performance is reported and compared to that of the inert conditions in glove box environment.

There were overall 12 series of samples fabricated, each consisting of 8 substrates. Each substrate consists of 4 solar cells. This makes an overall 96 complete substrates or 384 PSCs, of which 208 were mesoscopic PSCs and 192 were planar PSCs. In most of the cases, the results discussed throughout this chapter refer to the best performing cells of the series. Due to discrepancy in the quality of the perovskite layers in some of the samples, the overall device performance varies greatly in each series. The difficulty in achieving a reproducible set of high quality perovskite layers is a well-known issue in perovskite fabrication. However, when comparing the performance of homogeneous perovskite films, the photovoltaic response is comparable.

It was not observed any significant influence of the different FTO etching methods prior to cells fabrication on the final device performance. The mechanical etching is a faster and easier method compared to the chemical etching, and thus it is preferable.

5.1 Methyl Ammonium Lead Iodide Solar Cells

When $MAPbI_3$ was deposited by two-step sequential method straight on top of the TiO_2 compact layer, i.e. when fabricating a planar cell, a remarkably shrinking of the perovskite layer was observed during the annealing of perovskite. The shrinking was so extensive that the perovskite layer became unmeasurable and very uneven. The same $MAPbI_3$ deposition method has however been used for planar devices in glovebox with a great success numerous times. This highly indicates the sensitivity of the $MAPbI_3$ perovskite to moisture and oxygen during the fabrication process and the difficultness of the planar PSC fabrication in ambient conditions.

The 1-step antisolvent method with planar PSC, TiO_2 ETL, and $MAPbI_3$ perovskite was then studied. The TiO_2 compact layer was fabricated by spin coating as in the previous experiment and the perovskite was deposited on top of TiO_2 by 1-step antisolvent method. Anhydrous chlorobenzene was used as a solvent for spin coating. The perovskite layer remained on the samples and no shrinking was observed in this case. The perovskite layer

turned shiny light brown during the first ten minutes of annealing and when transferred to vacuum at 100 °C for 1 hour the light brown color remained and no degradation of perovskite was observed during the annealing. The picture of the cell is presented in Figure 10a. The best cell of the series achieved PCE of 3.89 %, as reported in the Table 4.

The same method was also tested exactly in the same way and with same materials, except with anhydrous toluene instead of chlorobenzene and with annealing in air instead of vacuum (Figure 10b). When annealed in air, the color of the perovskite appeared a little lighter, and the surface of the film was not shiny like in the previous time. The best cell of the series achieved PCE of 1.67 %, and it showed also a clear decrease in FF, J_{sc} and V_{oc} compared to the corresponding cells annealed in vacuum, as can be seen in the Table 4. The perovskite also started degrading already during the annealing, as evidenced by the color change from brown to yellow at the sample edges. The same behavior was observed for the same cell structure with SnO_2 ETL and $MAPbI_3$ annealing in vacuum. The best cell achieved a PCE of only 0.47 % and remarkable decrease in J_{sc} and V_{oc} compared to the cells with TiO_2 ETL. This refers to a hindered charge transfer in SnO_2 layer, possibly due to a pinholes and inhomogeneous ETL. This indicates the high sensitivity of $MAPbI_3$ perovskite to the moisture and oxygen during the crystallization process. The perovskite crystallization approaches the yellow phase in the presence of oxygen and moisture, and this causes decrease in cell performance. The light color of the perovskite also indicates that the 1-step antisolvent method with $MAPbI_3$ perovskite is an inappropriate fabrication method in ambient circumstances. When comparing the achieved results with one-step method and $MAPbI_3$ perovskite to the corresponding devices fabricated in glove box (Table 4), a remarkable difference in PCE and J_{sc} is observed. This supports the conclusion, that $MAPbI_3$ perovskite layer is very sensitive to ambient conditions.

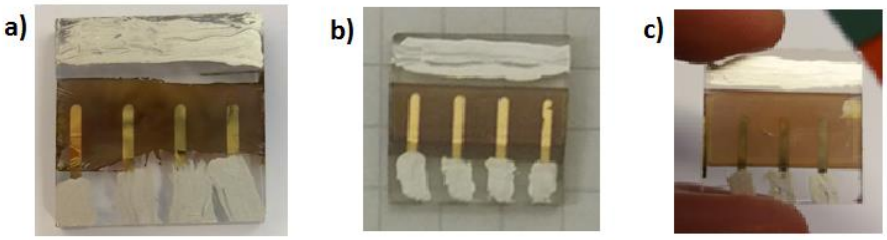

Figure 10. *Planar PSC with TiO_2 ETL and $MAPbI_3$ perovskite fabricated by 1-step antisolvent method and (a) annealed in vacuum and (b) annealed in air. (c) Planar PSCs with $MAPbI_3$ perovskite and SnO_2 ETL fabricated by 1-step antisolvent method and annealed in vacuum.*

Table 4. *Planar PSCs with MAPbI3 perovskite fabricated with one-step method, and TiO_2, or SnO_2 ETL fabricated by spin coating. The cells with annealing in "glove box" are reference cells from the literature, and have been fabricated in glove box.*

ETL	Annealing	Scan direc-tion	PCE [%]	FF [%]	J_{sc} [mA/cm^2]	V_{oc} [V]	*Ref.*
TiO_2	vacuum	forward	3.8949	46.822	9.0418	0.9200	-
		reverse	3.5233	50.893	7.7787	0.8900	-
SnO_2	vacuum	forward	0.4666	41.349	4.2571	0.2651	-
		reverse	0.0563	39.266	1.2521	0.1145	-
TiO_2	air	forward	1.6685	39.546	5.4695	0.7714	-
		reverse	1.2689	51.178	3.2142	0.7714	-
SnO_2	air	forward	0.3018	33.993	2.4208	0.3667	-
		reverse	0.0195	27.101	1.6761	0.0429	-
TiO_2	glove box	-	11.400	58.500	19.500	1.0000	[57]

The 2-step fabrication method of $MAPbI_3$ on top of the mesoporous TiO_2 layer, with both TiO_2 and SnO_2 compact ETL, resulted in improvement in homogenous and darker color of the shiny perovskite layer. For the $MAPbI_3$ with mesoscopic TiO_2 and TiO_2 ETL, and the perovskite annealing in vacuum, a PCE of 4.15 % was achieved, which is a bit higher compared to the respective planar device. In fact, an increase in FF was observed, but on the contrary the J_{sc} and V_{oc} moderately decreased. The cell is presented in Figure 11a, and the IV curves for the cell are depicted in Figure 12. The crack in the perovskite layer is the result of the uneven crystallization during the immersion in the MAI solution, after PbI_2 spin coating. The best performing cell did not show this kind of crack, but the figure of that device is presented to highlight the importance of steady sample dipping for the perovskite crystallization. The crack in the perovskite layer corresponds to a decrease in the cell performance due to restricted charge transport in the crack area.

The IV curves of the cell show very modest hysteresis effect despite the device was fabricated in ambient circumstances. This refers to a small difference in cell performance between the reverse and forward scan, and it is typical of mesoscopic PSCs as shown in Figure 7. Further tests, with the same device structure and with perovskite fabrication by 1-step method and subsequent annealing in air, consolidate the former observations on the inappropriateness of 1-step method with $MAPbI_3$ perovskite in ambient conditions. The resulting perovskite film shows a light color, and its surface turns out blurry during the annealing. The cell is presented in Figure 11b and the cell achieved a PCE of 1.00 % and a notable decrease in J_{sc} (2.77 mA/cm^2), and V_{oc} (0.65 V)

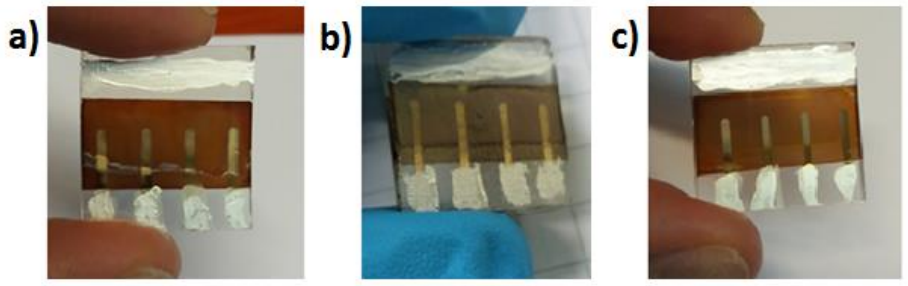

Figure 11. *Mesoscopic PSCs with $MAPbI_3$ perovskite and TiO_2 ETL fabricated by (a) two-step sequential method, (b) one-step antisolvent method and (c) SnO_2 ETL fabricated by two-step sequential method. Samples (a) and (c) were annealed in vacuum and (b) was annealed in air.*

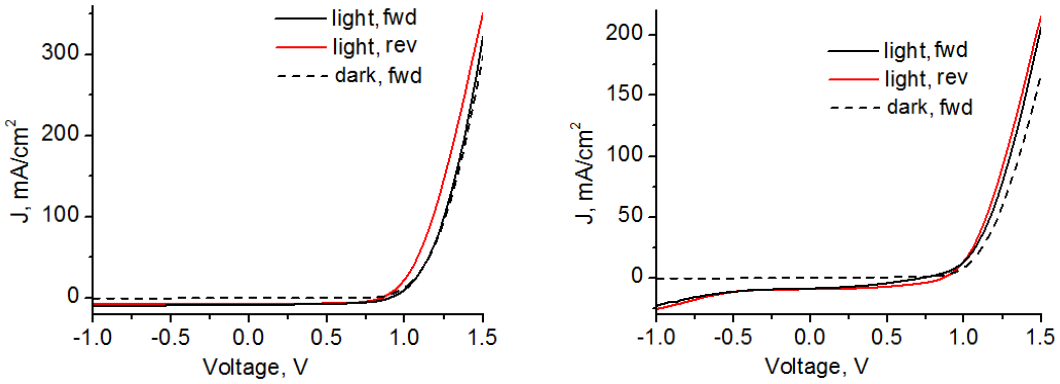

Figure 12. *IV curves for mesoscopic PSC with $MAPbI_3$ and TiO_2 (left) and SnO_2 (right) ETL. Forward scan is marked as fwd and reverse scan as rev.*

For the similar device structure with SnO_2 ETL, but with $MAPbI_3$ fabrication with 2-step method and annealing in vacuum, a PCE of 3.70 % was obtained. The cell with SnO_2 ETL also showed a decrease in FF and J_{sc} indicating the hindrance of charge transfer in SnO_2 compared to corresponding device with TiO_2. The cell is presented in Figure 11 c, and the IV curves measured for the cell are presented in Figure 12. A slightly lighter color of the perovskite in Figure 11c compared to 11a is observed, indicating the influence of different underlying ETL to the perovskite morphology. Since a darker color indicates a more complete crystallization, we can conclude that in ambient circumstances and with $MAPbI_3$ perovskite, the TiO_2 compact layer forms a better substrate for perovskite crystallization compared to SnO_2 compact layer. The IV curves for the cell show negligible hysteresis, but the bending of the curve at -1.0 V indicates imperfect diode behavior, which partially explains the weak cell performance. As expected by the material bandgaps presented in the Figure 4, the better matching bandgaps of TiO_2 and $MAPbI_3$ compared to $MAPbI_3$ and SnO_2 allow more effective charge transfer through the surface of the layers. This justifies the increased cell performance even in ambient conditions. In the Figure

11c, the crack in the Figure 11a is not observed due to a steady dipping in the MAI solution, and a homogenous perovskite layer results. The sensitivity of $MAPbI_3$ is observed for all samples by a slow degradation of perovskite layer after the cell fabrication. The $MAPbI_3$ perovskite layer starts turning from brown to yellow in the presence of ambient air in minutes.

For the SnO_2 compact layer, two different deposition methods were applied, namely spin coating and the combination of spin coating and CBD. The SEM images of the surfaces of SnO_2 layers fabricated by both deposition methods are presented in Figure 13. From the images we can see that the spin coated SnO_2 layer covers well the sample area but several pinholes are observed. The pinholes in the SnO_2 layer explain the poor charge transport and consequently the poor cell performance of the devices containing SnO_2 compact layer.

The image of the film obtained by the combined method on the other hand shows a very uneven SnO_2 layer on top of FTO. The SnO_2 is only partially found in separable small areas and it seems like CBD has diluted the spin coated layer from the FTO surface. This clearly explains the extremely poor cell efficiency of the devices with the maximum PCE of 0.01 % since the method results almost no ETL at all. The experiment was repeated and the new SEM images were taken to diminish the possibility of any error during the fabrication process but the same observation was concluded. For the corresponding method performed in inert conditions the combined method formed a thicker and pinhole free SnO_2 layer on the FTO surface, which differs greatly from the result achieved in this Thesis [37]. In spite of the careful repetition of the experiment, we could not reproduce the results in [37], due to possible inaccuracy in the description of the experimental conditions in the published work, or to the fact that we have prepared the films in ambient conditions. The rough ultrasonic bath treatment after the CBD deposition could be one reason for the disappearance of the SnO_2 layer in the combined method, and further attempts should include investigations without the ultrasonic bath. However, due to limited resources and time, the combined SnO_2 deposition method was not investigated in this Thesis, and in the following experiments SnO_2 was fabricated only by spin coating method.

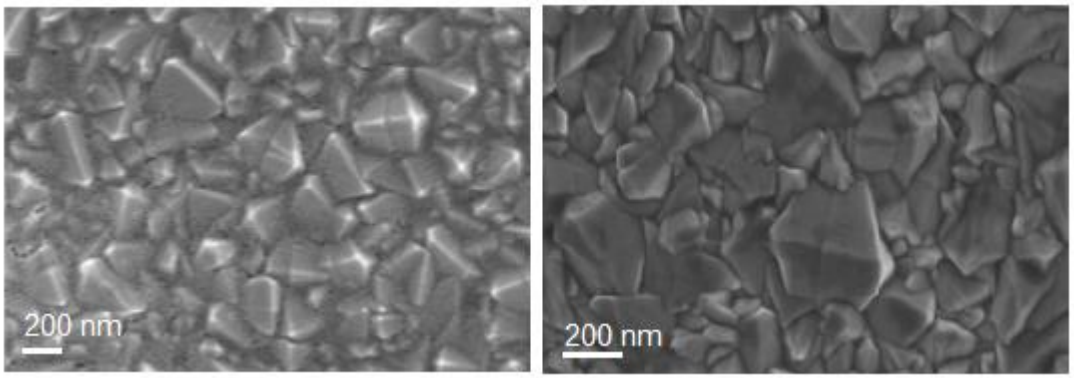

Figure 13. *SEM images of FTO with SnO_2 compact layer fabricated by spin coating (left) and CDB (right). The scale bar is 200 nm in both images.*

The achieved cell performance for both planar and mesoscopic PSCs with $MAPbI_3$ are far from the results achieved in inert fabrication conditions. For example, for a mesoscopic cell structure with a 2-step fabrication of perovskite and TiO_2 ETL, 15.0 % PCE has been achieved, as shown in Table 5. [42] When comparing these published data with those of the corresponding cell structure in the Table 5, we see that the results differ greatly in PCE, FF and J_{sc}. On the contrary the achieved V_{oc} 0.8952 V is close to the V_{oc} of high efficiency cells prepared in glove box.

Table 5. *Mesoscopic PSCs with $MAPbI_3$ perovskite fabricated with two-step method, and TiO_2, or SnO_2 ETL fabricated by spin coating. The cells with annealing in "glove box" are reference cells from the literature, and have been fabricated in glove box.*

ETL	Annealing	Scan direc-tion	PCE [%]	FF [%]	J_{sc} [mA/cm^2]	V_{oc} [V]	*Ref.*
TiO_2	vacuum	forward	4.1519	55.189	8.4036	0.8952	-
		reverse	3.7524	67.776	6.7974	45.000	-
SnO_2	vacuum	forward	2.3000	37.966	8.7353	0.6935	-
		reverse	3.7008	45.804	9.4522	0.8548	-
TiO_2	glove box	-	15.000	73.000	20.000	0.9330	[42]

The stability of mesoscopic PSCs with $MAPbI_3$ was successfully enhanced by controlling the thickness of mesoporous TiO_2 layer fabrication in ambient fabrication circumstances. This was performed by different numbers of spin coating cycles. With optimized layer thickness, the cells maintained 85 % of their initial PCE after 100 days. This might be due to the protected crystallinity and charge transportation channels induced by the mesoporous layer. [58] Efficient mesoscopic cells were fabricated in ambient air by modified spin coating method, and by replacing two I^- from the $MAPbI_3$ formula with SCN^-. These

cells achieved PCEs up to 15 %, and showed a good stability. [59] With two-step sequential method, ~15 % PCE in ambient air has been reported. In the research work, the faster spin program speed for the deposition of PbI_2 was found critical for high quality film formation. [60] There are also some reports about the stabilization of planar PSCs applying $MAPbI_3$, but clearly fewer compared to mesoscopic structure, which could refer to the difficulty of fabricating planar PSCs in ambient air. However, a PCE of 12.98 %, with a planar device in ambient air has been reached. The device was fabricated by one-step method, and with mixed halide $CH_3NH_3PbI_{3-x}Cl_x$ perovskite. In the fabrication process, the vacuum annealing was introduced to perovskite fabrication, and it was reported to enhance the cell performance and stability. [61]

5.2 Triple Cation Solar Cells

The triple cation perovskite was fabricated only by 1-step antisolvent method. The generic form of the investigated triple cation perovskite is $Cs_x(MA_{0.17}FA_{0.83})_{(100-x)}Pb(I_{0.83}Br_{0.17})_3$ where x is percentage. The triple cation recipes are $Cs_5(MA_{0.17}FA_{0.83})_{95}Pb(I_{0.83}Br_{0.17})_3$ for 0.05 M Cs perovskite solution, or $Cs_9(MA_{0.17}FA_{0.83})_{91}Pb(I_{0.83}Br_{0.17})_3$ for 0.08 M Cs perovskite solution, marked as Cs_5M and Cs_9M respectively. The experiments with triple cation perovskite were started with Cs_5 M and later the influence of the increase in Cs concentration was studied by adding Cs as in Cs_9M. At first, triple cation perovskite was fabricated on pure FTO and the resulting shiny and dark perovskite layers are presented in Figure 14. The dark color of perovskite appeared immediately after the solvent deposition (anhydrous chlorobenzene or anhydrous toluene) during spin coating of the perovskite layer, indicating a rapid crystallization process in the presence of Cs in perovskite solution.

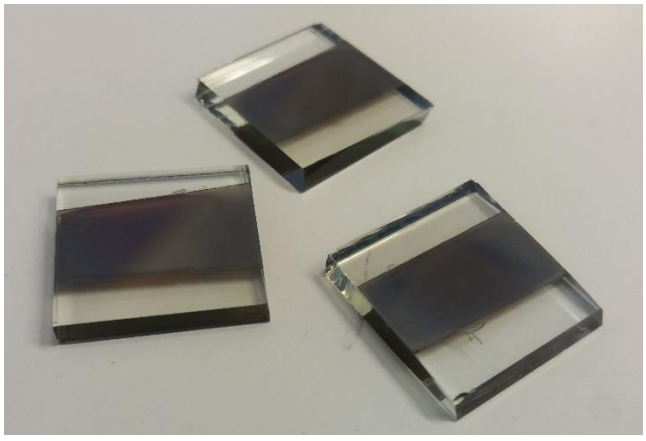

Figure 14. *Cs/MA/FA triple cation perovskite layer on top of pure FTO.*

When the triple $Cs_{1.5}M$ perovskite was deposited on top of TiO_2 mesoporous layer, on TiO_2 or SnO_2 compact ETL, a much lighter brown color was observed. In this case, the brown color appeared immediately after solvent pipetting on the samples, and the perovskite surface was shiny. Interestingly the brown shiny layer did not cover the complete

cell area in any of the fabricated cells, but the perovskite layer seemed to cover only the middle of the samples as seen in Figure 15. To the best of my knowledge, this kind of behavior has not been reported before. The lack of the reports on this kind of behavior could be due to an absence of experiments on the triple cation perovskite fabrication in the presence of ambient air and humidity. The behavior could arise from the modest sensitivity of the triple cation perovskite to humidity and/or oxygen, and the inappropriateness of the 1-step method in ambient circumstances.

The use of anhydrous solvent in 1-step antisolvent method is important for the perovskite crystallization [11]. In ambient conditions, the benefit of anhydrous solvent is diminished, and humidity is damaging the perovskite morphology. This would also partially explain the light color of the perovskite layer but does not explain the color difference of the perovskite deposited on top of FTO and on compact/mesoporous oxide layer, raising questions on the quality of the compact layer. The size of the uniform and shiny perovskite layer also varied a lot even within the same series. This could stem from the sensitivity of MA/FA to the temperature at the beginning of the crystallization, since even small temperature changes have been reported to affect the crystallization of the black phase of FA. Also the solvent vapors and humidity affect the MA/FA perovskite composition and the used amount of cesium was not enough to stabilize sufficiently the perovskite formation. [25] This behavior was observed with both cesium concentrations and also a “hole” in the middle of the perovskite layer was easily observed in the perovskite layer, as presented in Figure 15d. The hole is formed during the solvent pipetting at perovskite layer fabrication. It is possible to avoid by extremely precise pipetting on the exactly correct height and as a steady flow as seen on Figures 15a-c. The hole formation on the perovskite decreases the cell performance the same way as the cracks in the case of the 2-step sequential method.

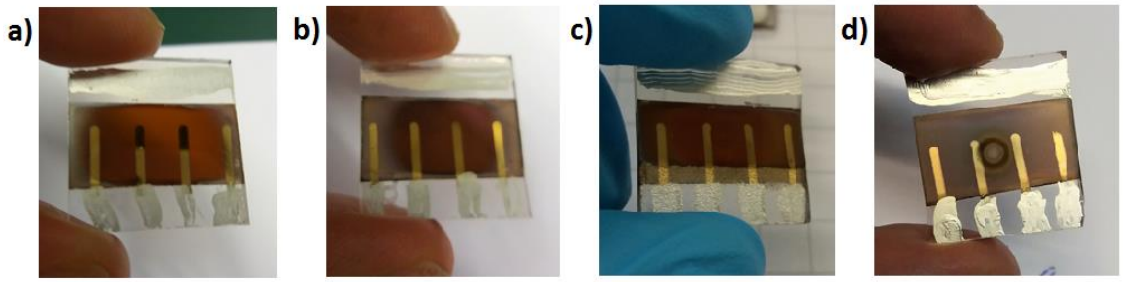

Figure 15. *Planar PSCs with Cs/MA/FA triple cation perovskite and (a) TiO_2 ETL and (b) SnO_2 ETL and mesoscopic PSCs with Cs/MA/FA triple cation perovskite and (c) TiO_2 ETL and (d) SnO_2 ETL. All cells (a-d) were fabricated by one-step antisolvent method.*

The best performing planar and mesoscopic PSCs with triple cation perovskite for both TiO_2 and SnO_2 ETLs are presented in Table 6. From the table we can see that the best planar device with TiO_2 ETL achieved 5.70 % PCE in forward, and 9.88 % in reverse

scan, which is the record efficiency in this Thesis. The best performing mesoscopic cell with TiO_2 ETL achieved 7.38 % PCE and 7.07 % respectively to forward and reverse scans. The bigger differences in the results of forward and reverse scan for planar device indicate a greater hysteresis effect. The FFs are in average higher for mesoscopic devices, (FF ~60 %), which is considered quite high even for state-of-the-art PSCs. On the other hand, the V_{oc} is on average greater for planar cells. J_{sc} varies between 5.47 and 15.34 mA/cm^2 depending on the cell structure, on ETL, and on the perovskite annealing treatment. The difference between TiO_2 and SnO_2 ETLs is discussed in detail in the next chapter.

Table 6. *Planar PSCs with triple cation perovskite and TiO_2, or SnO_2 ETL, fabricated by spin coating. The cells with annealing in "glove box" are reference cells from the literature, and have been fabricated in glove box.*

ETL	structure/ annealing	Scan direction	PCE [%]	FF [%]	J_{sc} [mA/cm^2]	V_{oc} [V]	*Ref.*
TiO_2	planar/ vacuum	forward	5.6997	64.069	12.828	0.6935	-
		reverse	9.8773	60.509	14.883	1.0968	-
SnO_2	planar/ vacuum	forward	3.0418	41.918	6.8685	1.0565	-
		reverse	4.5983	59.791	8.2209	0.9355	-
TiO_2	meso/ vacuum	forward	6.4590	57.727	14.452	0.7742	-
		reverse	5.3781	53.453	12.997	0.7742	-
SnO_2	meso/ vacuum	forward	1.0442	41.930	9.9615	0.2500	-
		reverse	0.9625	43.212	8.9098	0.2500	-
TiO_2	meso/ air	forward	7.3837	66.496	12.409	0.8952	-
		reverse	7.0718	65.464	12.067	0.8952	-
TiO_2	meso/ N_2	forward	5.7121	61.288	11.443	0.8145	-
		reverse	4.3842	58.176	9.7340	0.7742	-
TiO_2	meso/ glove box	-	19.200	74.800	22.690	1.1320	[25]
SnO_2	planar/ glove box	-	19.210	77.000	22.370	1.1800	[37]

The IV curves for mesoscopic and planar devices with triple cation perovskite are presented in Figure 16. As can be seen from both the measurements, the shape of the curves are good, thus indicating good FFs and the negligible hysteresis for both devices. The reproducibility of the cells also improved when choosing the mesoscopic architecture and triple cation perovskite. This result supports the more suitable fabrication of mesoscopic devices by solution process, discussed in chapter 3.3.2, and of the robustness of triple cation perovskite. When compared to the mesoscopic device with $MAPbI_3$ perovskite and

TiO_2 ETL presented in Figure 12, the hysteresis observed is even smaller for the corresponding device with triple cation perovskite. This indicates good contact area between perovskite and the mesoporous layer and thus good charge transport. The increase of Cs concentration on the cell performance was negligible in all cell configurations.

As opposite to the $MAPbI_3$ devices, the average PCE, and especially V_{oc} of triple cation devices, increased slightly when the perovskite layer was annealed in air with respect to the annealing in vacuum. This can be seen also from the Table 6: the best performing mesoscopic cells were annealed in air. This is a very interesting result and highlights the robustness of triple cation perovskite to ambient conditions. However, the best planar device was annealed in vacuum. From this we can conclude that in planar cell architecture the perovskite layer could be more sensitive to ambient conditions. The annealing of the corresponding devices in inert conditions (in N_2 atmosphere) slightly increased the cell performance and the J_{sc} but, due to reproducibility issues and lack of repetition, this experiment would demand additional research work and should be studied for different cell configurations i.e. also for planar cells. Due to the lack of proper equipment, the annealing in N_2 was performed only for one series.

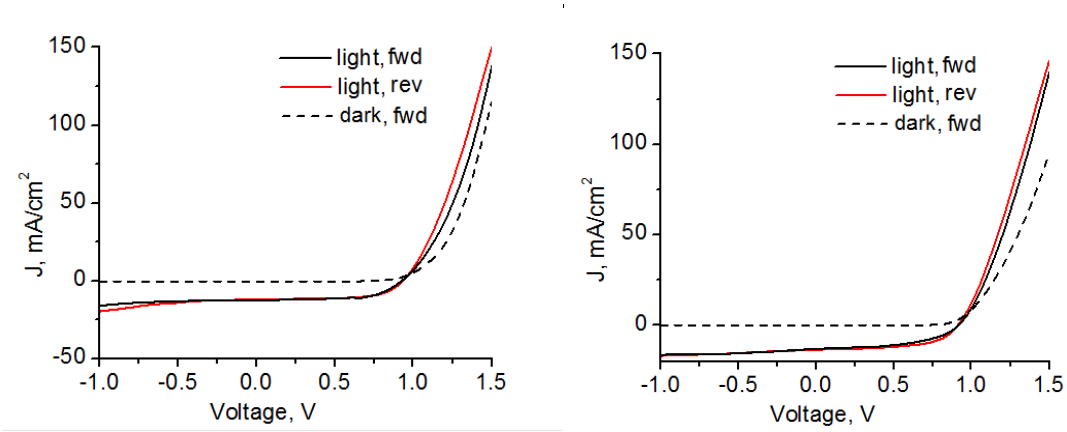

Figure 16. *IV curves for mesoscopic (left) and planar (right) PSCs with Cs/MA/FA triple cation perovskite and TiO_2 ETL fabricated by spin coating.*

The cross section SEM images of the mesoscopic and planar PSCs, with the triple cation perovskite and TiO_2 ETL, are presented in Figure 17. The TiO_2 was fabricated by spray pyrolysis, and the mesoporous layer was fabricated by spin coating from 30 NR-D titania paste. The SEM images for both the devices show a good uniform ETLs and well crystallized and consistent perovskite layers. The average layer thicknesses in mesoscopic device were determined as 30 nm for the ETL, 180 nm for the mesoporous layer, 220 nm for the perovskite layer, and 220 nm for the HTL. For planar device, the thicknesses are 30 nm for ETL, 300 nm for perovskite, and 220 nm for HTL. It is interesting to notice in the pictures the differences in the spiro-OMeTAD layer. The spiro-OMeTAD in the planar device is pinhole-free and uniform as it is expected to be, but the spiro-OMeTAD layer in the mesoscopic device has holes in it. Both of the samples were fabricated on the

same day from the same solutions so the influence cannot be due to the errors in solution preparation. The spiro-OMeTAD is known to oxidize in the presence of oxygen and humidity, and the samples were stored in the desiccator cabinet (10 % rH) for two weeks before imaging, but this still does not explain the difference in these two samples. However, the image was taken only on one sample and, in order to study this phenomenon thoroughly, several samples should be studied to exclude errors in the fabricating process.

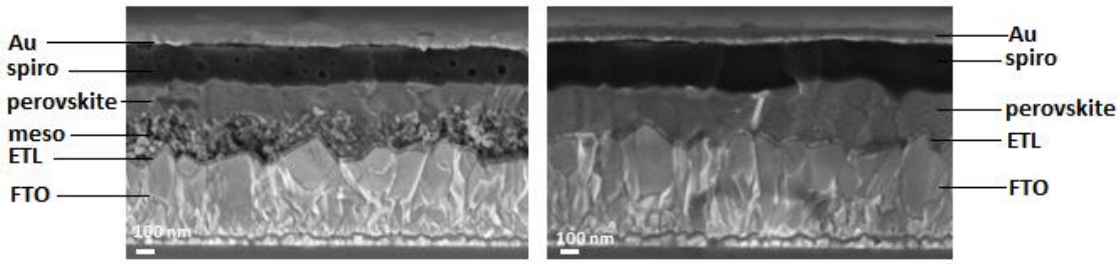

Figure 17. *Cross-section SEM image of mesoporous FTO/bl-TiO_2/mp-TiO_2/(Cs/MA/FA)/* spiro-OMeTAD */Au (left) and planar FTO/bl-TiO_2 /(Cs/MA/FA)/* spiro-OMeTAD */Au (right) solar cell. The scale bar for both images is 100 nm.*

Compared to the devices containing $MAPbI_3$ perovskite, the cell performance of the triple cation-based perovskite composition is remarkably higher. With the best performing cells fabricated by 1-step method, the increase in PCE for planar devices is 39 % and for mesoscopic cells even 56 %. The FF of the triple cation perovskite devices is on average higher and good for both device structures. J_{sc} shows great increase with triple cation devices from 9.04 mA/cm^2 to 15.34 mA/cm^2 for planar devices, and from 2.77 mA/cm^2 to 12.41 mA/cm^2 for mesoscopic devices. V_{oc} for planar devices increased only slightly for the best planar devices, from 0.92 V to 0.9738 V but a much greater increase in the case of mesoscopic devices was observed from 0.69 V to 0.90 V. The samples with triple cation perovskite and TiO_2 ETL maintain the brown color in ambient air for weeks without evident color change to yellow. As expected, this highly indicates the robustness of triple cation perovskite in ambient fabrication circumstances compared to $MAPbI_3$. Even though the improvement in the cell performance is remarkable for the triple cation perovskite devices, they are still far behind the PCE of corresponding cells fabricated in inert circumstance. For a Cs_5M triple cation perovskite fabricated by 1-step method in glove box, average results reported in the literature are 19.20 %, 74.80 %, 22.69 mA/cm^2, and 1.13 V, for PCE, FF, J_{sc}, and V_{oc} respectively [25]. The FF and V_{oc} achieved in this Thesis are close to the values of published high-efficiency cells, but a notable decrease in PCE and J_{sc} is observed. These results suggest that 1-step method might not be a suitable fabrication method for high-efficiency PSCs in ambient circumstances, and that the cesium concentration in the studied perovskite material should be still increased.

To my best knowledge, reports on Cs/MA/FA triple cation perovskite fabricated in ambient air have not been published by so far. There are though some reports about fabricating mixed cation MA/FA PSCs in ambient air. With a $MA_XFA_{1-X}PbI_3$ perovskite, planar device, and a low pressure CVD deposition method a PCE of 15.86 % and a good stability was achieved. [62] Mixed $(FAPbI_3)_{1-x}(MAPbBr_3)_x$ perovskite applied to mesoscopic cell structure was fabricated in ambient air with one-step antisolvent reaching 18.8 % PCE. This was achieved by pre-heating the spin coated substrate before perovskite deposition and optimizing the heating temperature to 50 °C. [63] These methods could be applied also to triple cation perovskite to enhance the cell performance in ambient fabrication conditions.

5.2.1 Influence of Electron Transport and Mesoporous Layers

As shown for the devices with $MAPbI_3$, the difference in TiO_2 and SnO_2 ETLs is remarkable also in triple cation devices with both planar and mesoscopic cell structures. From the table in Appendix A we see that the highest PCE for the planar device with triple cation perovskite and SnO_2 ETL fabricated by spin coating is 4.60 % and for mesoscopic device 1.04 %. The corresponding PCE for the devices with TiO_2 ETL fabricated by spin coating are 9.88 % and 7.38 %. The FF and J_{sc} of the devices with TiO_2 are clearly higher, while the average V_{oc} for the planar device with SnO_2 is only slightly higher. The higher PCE, FF, and J_{sc} refer to better charge transfer and contact in the surface area between ETL and perovskite layers. This result is opposite to what was expected due to better matching bandgaps of SnO_2 and the triple cation perovskite, but could be explained with the layer uniformity seen in the SEM images of the fabricated TiO_2 and SnO_2 layers. The SEM image of SnO_2 surface is presented in Figure 13, and the image of TiO_2 surface is presented in Figure 18. Comparing the surface images, the reduced amount of pinholes in TiO_2 layer is observed. The thickness of both layers fabricated by spin coating were determined to be 20 - 90 nm for SnO_2 and 40 - 50 nm for TiO_2. The thicknesses were determined by cross sectional SEM images. The wide variation in SnO_2 layer thickness also partially explains the poor cell performance.

The IV curves for the mesoscopic and planar devices with SnO_2 ETL are presented in Figure 19. The curves for both devices show a modest bending of the curve at -1.0 V indicating nondeal diode behavior, and the steep linear rise in the curves of mesoscopic device could arise from the device degradation during the measurement. The IV curves of the planar device display a better FF but a notable hysteresis and fluctuation in the reverse curve is observed. When comparing the curves of Figure 19 to the corresponding curves of the devices with TiO_2 ETL shown in Figure 16, the observations of diminished hysteresis and the FF of the curves for TiO_2 devices support the results of better cell performance in the case of TiO_2 ETL. Due to the demonstrated weak influence of SnO_2 ETL on the cell performance, the remaining experiments were performed only with TiO_2 ETL.

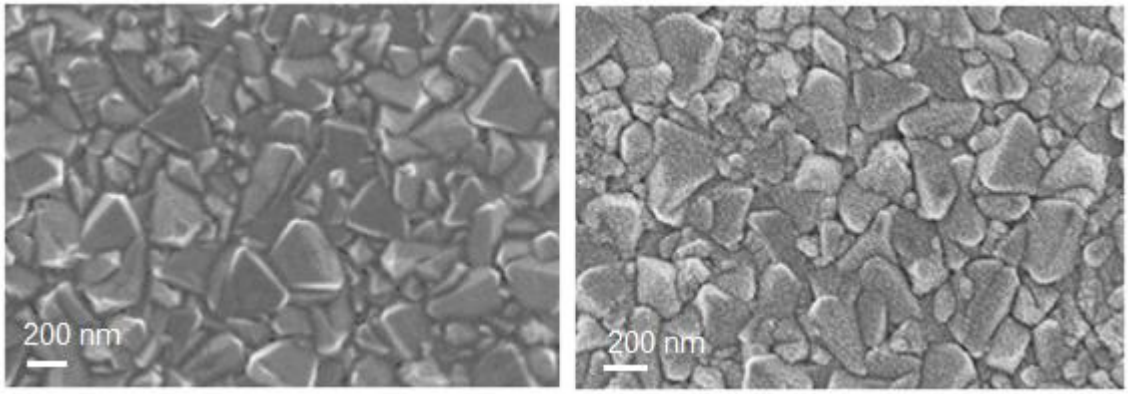

Figure 18. *SEM images of TiO_2 surfaces on FTO fabricated by spin coating (left) and spray pyrolysis (right). The scale bar is 200 nm in both images.*

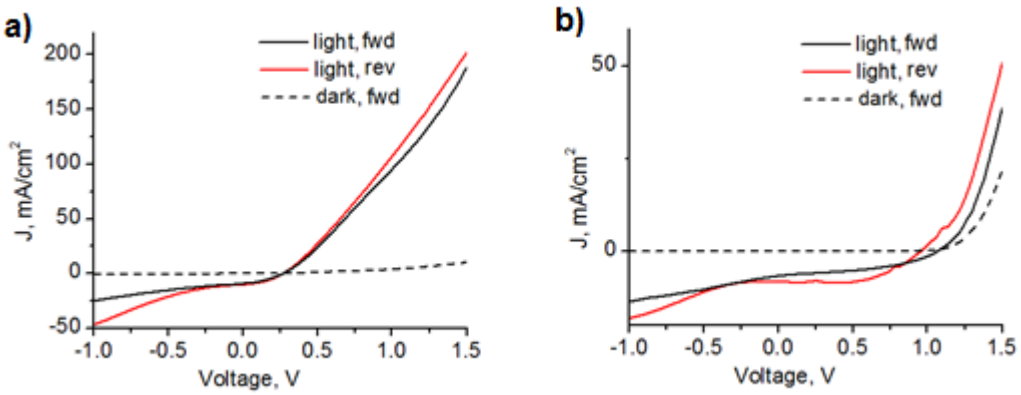

Figure 19. *IV curves for PSC with triple cation perovskite, SnO_2 ETL and (a) mesoscopic and (b) planar cell structures.*

As mentioned in chapter 3.2.1, spray pyrolysis is a well-known method for TiO_2 fabrication for preparing high-quality, crystalline thin films [38]. Thus, we decided to compare the influence of spray pyrolyzed TiO_2 ETL to the cell performance of our PSCs. The spray pyrolyzed TiO_2 ETLs were fabricated in the University of Cologne through the collaboration with AK Mathur group. The SEM image of the spray pyrolyzed TiO_2 surface is presented in Figure 18. The surface seems to be pinhole free and uniform. The thickness of the layer was determined from the cross sectional SEM image and it is ~30 nm and shows only modest thickness variation. The uniform layer and the absence of pinholes explain the good cell performance shown in the Table 7.

Table 7. *Planar and mesoscopic PSCs with triple cation perovskite, annealed in air, and TiO_2 ETL, fabricated by spray pyrolysis.*

Cell architecture	titania paste	Scan direc-tion	PCE [%]	FF [%]	J_{sc} [mA/cm^2]	V_{oc} [V]
planar	-	forward	6.0422	40.4439	15.3417	0.9738
		reverse	7.9402	54.5120	14.9579	0.9738
mesoscopic	18 NR-T	forward	4.2980	58.6375	9.0279	0.8119
		reverse	3.3361	76.4943	5.6536	0.7714
mesoscopic	30 NR-D	forward	5.4199	55.0378	11.5529	0.8524
		reverse	2.6344	55.1614	5.8822	0.8119

The IV curves of the best device with spray pyrolyzed TiO_2 (PCE of 6.04 % in forward scan, and 7.94 % in reverse scan) are presented in Figure 20a. The corresponding IV curves for the mesoscopic devices with mesoporous layer fabricated from 30 NR-D and 18 NR-T titania pastes are presented in Figures 20b and 20c, respectively. The planar curves show remarkable hysteresis, which is also reflected in the significant variation in the PCE between forward and reverse scans. The shape of the curves is relatively poor compared to corresponding device with TiO_2 fabricated by spin coating (Figure 16). The cells with spray pyrolyzed TiO_2 layer achieved lower PCEs than the corresponding cells with spin coated TiO2. On the other hand, FFs, J_{sc}, and V_{oc}, were high compared to the rest of the cells fabricated in the Thesis, as can be seen in the table in Appendix A.

The spray pyrolyzed TiO_2 was applied in only one series and, in order to get reliable results, the experiment should be repeated several times. The mesoscopic PSCs curves show a smaller hysteresis than planar devices, in agreement with what is found in the literature. The difference between the samples with 30 NR-D and 18 NR-T pastes are discussed shortly at the end of this chapter. The best performing mesoscopic cell architectures for both $MAPbI_3$ and triple cation perovskite, and the cell performances for devices with 18 NR-T and 30 NR-D titania pastes, are separated and presented in the table in Appendix A.

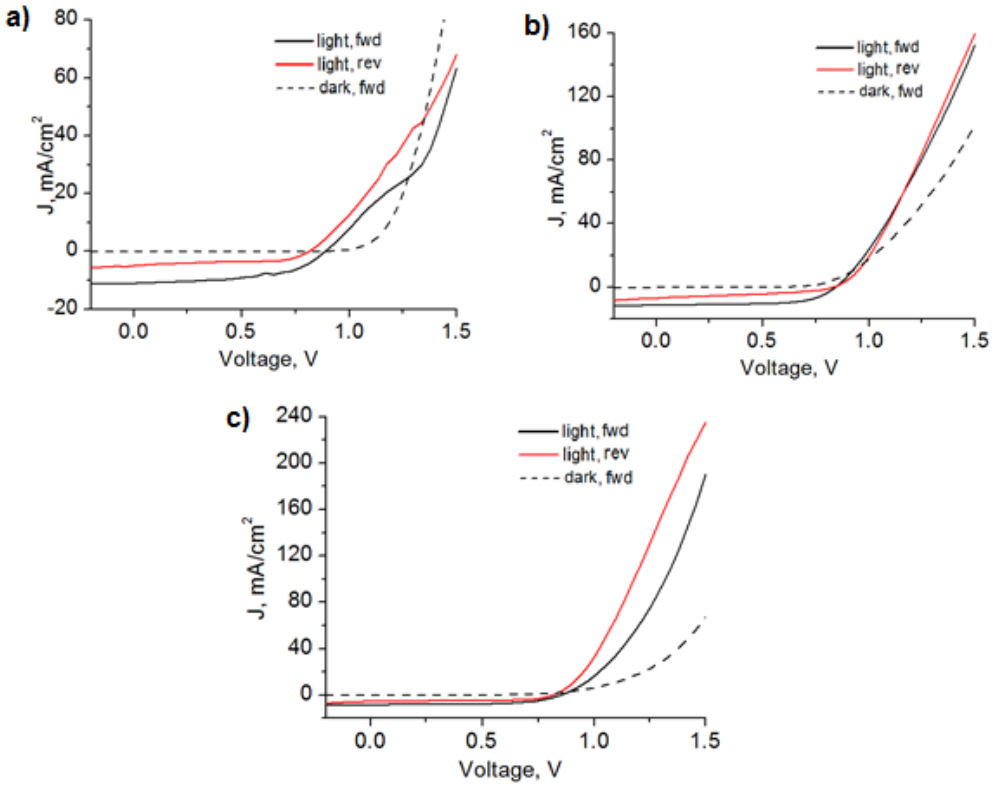

Figure 20. *IV curves for PSC with triple cation perovskite and TiO_2 ETL fabricated by spray pyrolysis and (a) planar cell architecture and mesoscopic cell architecture fabricated from (b) 30 NR-D paste and (c) 18 NR-T paste.*

With the aim of ruling out all the potential responsibles of the poor efficiencies of our PSCs, the quality of our ETLs was also investigated in co-operation with the University of Cologne. Our TiO_2 and SnO_2 compact layers were shipped to Cologne group, where the devices were completed with the remaining layers in glove box. In the other words, triple cation perovskite, spiro-OMeTAD HTL, and Au were deposited on top of the ETLs fabricated at TUT. The results for the best performing cells for both planar and mesoscopic devices are presented in Table 8. As can be seen, the values of all the photovoltaic parameters for both planar and mesoscopic cells with TiO_2 ETL approach the values measured for the state-of-the-art PSCs. This highly indicates that the fabricated TiO_2 ETLs are of high quality, and the fabrication of ETL in ambient conditions is not responsible for the poor overall cell performance. The critical step of the cells fabrication is the deposition of perovskite, which seems to be clearly dependent on the fabrication circumstances. Inert conditions clearly favor a smooth and well-controlled crystallization of perovskite crystals. The results in the Table 8 also prove that the ETL layers retain good quality for days, when stored in vacuum. The results for the planar device with SnO_2 ETL show clearly lower PCE and V_{oc} when compared to device with TiO_2 ETL. However, the FF and J_{sc} values are almost comparable.

Table 8. *The PCE, FF, J_{sc} and V_{oc} for the best planar and mesoscopic cells with triple cation perovskite and spiro-OMeTAD HTL fabricated in glove box at the University of Cologne. Measurements and fabrication were carried out by AK Mathur group and Dr. Vivo.*

Cell architecture	ETL	Scan direction	PCE [%]	FF [%]	J_{sc} [mA/cm^2]	V_{oc} [V]
planar	TiO_2	forward	18.773	67.677	25.494	1.0880
		reverse	20.099	68.547	26.844	1.0922
planar	SnO_2	forward	9.9580	58.477	21.992	0.7743
		reverse	14.808	69.792	25.018	0.8480
mesoscopic	TiO_2	forward	17.732	67.167	25.080	1.0526
		reverse	20.621	73.498	25.322	1.1079

The IV curves for the cells presented in Table 8 are shown in Figure 21. The IV curves for both planar and mesoscopic devices with TiO_2 show a good sharp shape and, as typical for planar devices, the hysteresis is slightly greater than for mesoscopic PSCs. For planar device with SnO_2 ETL, the hysteresis is modest but the shape of the curves are a little worse as can be noticed at high voltages (Figure 21b). By comparing the IV curves in Figure 21 and the IV curves of the corresponding devices fabricated in ambient air shown in Figures 19 and 20, it is safe to say that the hysteresis effect does not increase for the devices with TiO_2 ETL fabricated in ambient circumstances. On the other hand, the hysteresis on the planar device with SnO_2 ETL seems to increase slightly.

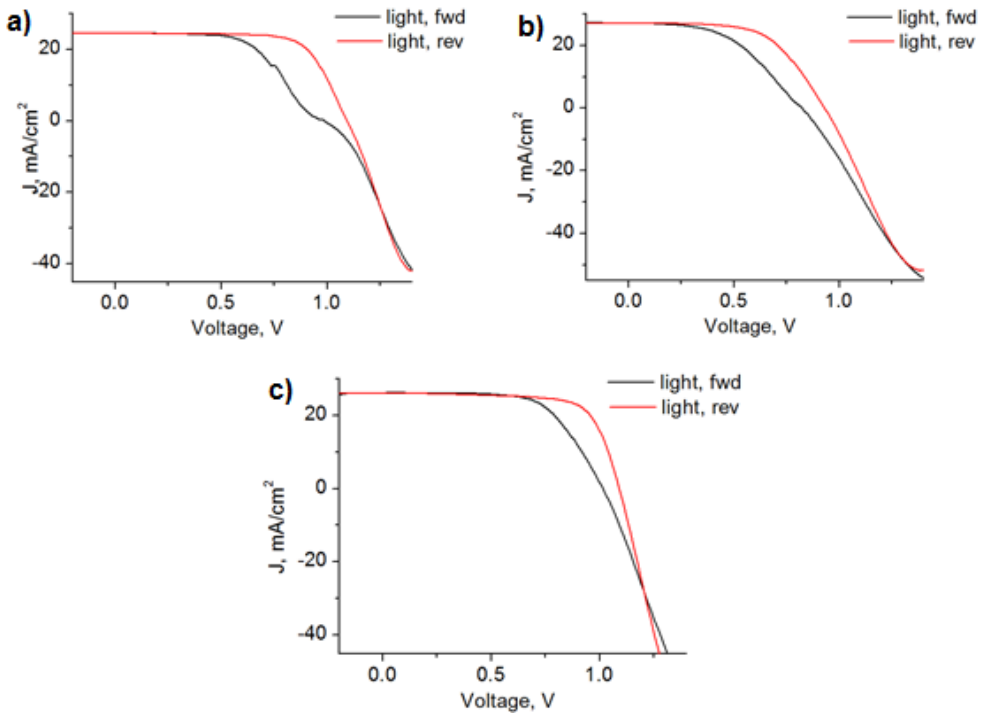

Figure 21. *IV curves for the planar PSCs with (a) TiO_2 and (b) SnO_2 and (c) mesoscopic device with TiO_2 ETL fabricated in glove box.*

Finally, the stability of the best performing cell architectures with triple cation perovskite were studied. These cell structures include planar PSC with TiO_2 ETL, and mesoscopic PSCs with mesoporous layer fabricated from 30 NR-D and 18 NR-T titania pastes. The mesoscopic devices fabricated from different titania paste are reported separately, since the difference between the two devices were noticed during the experiments. The IV curves for several cells were measured multiple times during a time period of 550 hours, and the average of the normalized results for the measured PCE, FF, J_{sc} and V_{oc} are presented with respect to time in Figure 22. The samples were re-stored in dark at room temperature and ambient humidity of 10 % rH between the measurements.

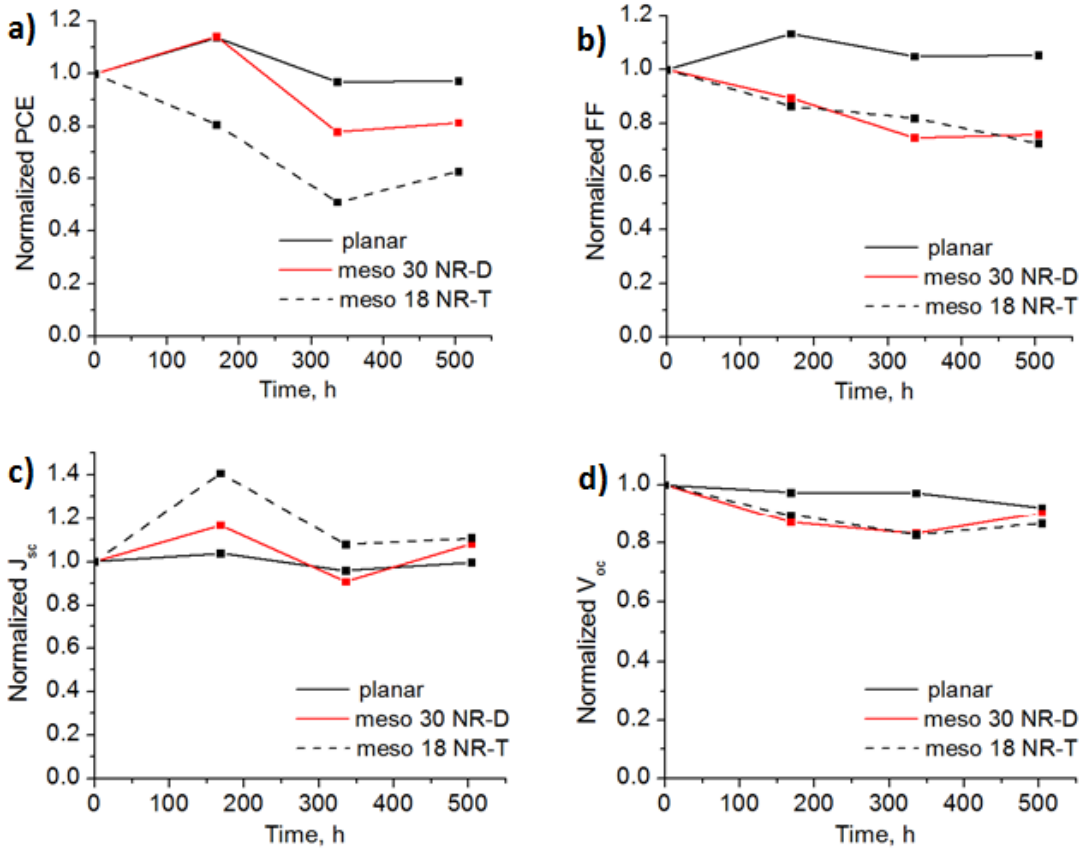

Figure 22. *Normalized (a) PCE, (b) FF, (c) J_{sc} and (d) V_{oc} for planar and mesoscopic PSCs with triple cation perovskite and TiO_2 ETL. The meso 30 NR-D paste indicates that the mesoporous layer was fabricated from 30 NR-D paste, and meso 18 NR-T that the mesoporous layer was fabricated from 18 NR-T paste. The ageing was performed in darkness in 10 % rH and 21 °C.*

For planar devices, all the photovoltaic parameters rise at first, and then show only a moderate decrease after 500 hours. After 500 hours, the normalized PCE with standard deviation for planar devices is 0.97 ± 0.28, FF is 1.05 ± 0.06, J_{sc} is 0.92 ± 0.20, and V_{oc} is 0.92 ± 0.20. This indicates good cell stability, and that long-lasting cells can be fabricated in ambient circumstances. The high standard deviations are due to reproducibility issues of the perovskite but, due to several samples tested, it is safe to assume the values indicate the average trend for the corresponding sample configurations. The phenomenon of increased cell performance during re-storing in the dark has been reported only recently [37, 64]. This suggests that PSCs may be able to reach full recovery in the natural working environment of solar cells during the day and night cycle, which would be a remarkable interesting property for highly efficient PSC.

The mesoscopic devices show similar behavior as concerning FF and V_{oc}. Interestingly, the PCE remains clearly higher for samples with 30 NR-D TiO_2 paste, and the J_{sc} increases more for the samples with 18 NR-T TiO_2 paste at first. The curves in both cases

have similar FF, though. For mesoscopic devices with 18 NR-T titania paste, the corresponding values are 0.63 ± 0.16 for PCE, 0.72 ± 0.01 for FF, 1.11 ± 0.27 for J_{sc}, and 0.87 ± 0.14 for V_{oc}. Respectively for mesoscopic samples with 30 NR-D titania paste, the values are 0.81 ± 0.18 for PCE, 0.76 ± 0.20 for FF, 1.08 ± 0.29 for J_{sc} and 0.90 ± 0.11 for V_{oc}. The real values (not-normalized) for devices with 30 NR-D titania paste show higher PCE and J_{sc} compared to devices with 18 NR-T titania paste. The FF and V_{oc} are similar for both. The thickness of the mesoporous layer with 30 NR-D titania paste was measured with cross sectional SEM imaging and it was determined to be 180 nm. The thickness of the mesoporous layer with 18 NR-T titania paste, with the applied spin coating parameters is estimated to be 400 nm. The lower efficiencies for the devices with 18 NR-T titania paste can be affected by the remarkably thicker mesoporous layer, which could hinder the electron transfer through it to the electrode and due to the smaller nanoparticle size. The bigger nanoparticles in 30 NR-D titania paste could form less grain boundaries compared to smaller nanoparticles, which could form a smoother mesoporous layer with less defects.

6. CONCLUSIONS

This Thesis was carried out at the Supramolecular Photochemistry Research Group, Laboratory of Chemistry and Bioengineering, TUT. The key results will be disseminated via poster presentation at the International Conference on Hybrid and Organic Photovoltaics (HOPV17) in Lausanne, Switzerland, in May 2017. The purpose of this Thesis is to compare the influence of ambient and inert PSCs fabrication. For both planar and mesoscopic cell architectures, different perovskite layers, in terms of composition ($MAPbI_3$ and Cs/MA/FA triple perovskites) and annealing conditions of the perovskite films, have been investigated. Additionally, two different ETLs, TiO_2 and SnO_2, were studied with different fabrication methods. This was the first time that the planar PSCs and devices based on the triple cation perovskite were fabricated at TUT. The achieved results include the current PCE-record of the group (9.88 %) with the new state-of-the-art solar simulator available.

It was proven that $MAPbI_3$ is very sensitive to ambient fabrication conditions. The one-step antisolvent method for both, TiO_2 ETL (3.89 % PCE), and SnO_2 ETL (0.47 % PCE), showed clearly poorer results compared to two-step method (4.15 % PCE for TiO_2 ETL, and 3.70 % PCE for SnO_2 ETL) and the fabrication of planar cells was harder than the fabrication of mesoscopic cells in ambient air. The perovskite layers showed a very light brown color instead of the typically dark brown color, thus indicating its incomplete crystallization. The enhanced results, more than doubled in PCE, and two times higher in J_{sc}, were observed when the perovskite layer was annealed in vacuum compared to annealing in air. The samples also started degrading in minutes in ambient air. The best planar device achieved a PCE of 3.89 % and the best mesoscopic device 4.15 %, which are both far from the corresponding devices fabricated in inert conditions. The state-of-the-art PCE and J_{sc} for PSC with $MAPbI_3$ and TiO_2 ETL are 15.0 % and 20.0 mA/cm^2, which is two-to-three times higher than the achieved results here. This indicates the inappropriateness of $MAPbI_3$ perovskite fabrication in ambient conditions.

The use of Cs/MA/FA triple cation perovskite had a clear improvement on the cell performance and on the device stability. This was already evident when comparing the color of the perovskite film, darker for the triple cation composition compared to devices with $MAPbI_3$. A shiny, very dark brown perovskite layer was observed when fabricating the perovskite on top of pure FTO. The dark perovskite and good cell performances indicate that fabricating PSCs with triple cation perovskite and high efficiency in ambient conditions could be possible. The lighter color of perovskite on top of compact or mesoporous layer though is a sign that alternative deposition methods in ambient conditions should be studied. The best performing samples with triple cation perovskite reached PCEs of 9.88 % (60.5 % FF, 14.88 mA/cm^2 J_{sc}, and 1.10 V V_{oc}) for planar, and 7.38 % (66.50 %

FF, 12.41 mA/cm^2 J_{sc}, and 0.90 V V_{oc}) for mesoscopic device and the devices showed only a modest hysteresis. The FFs and V_{oc} of the devices exceeded the corresponding values of high efficiency PSCs but the J_{sc} was modest. The best planar devices were annealed in vacuum, and showed 20 % enhancement in PCE, when compared to annealing in air. However, the best mesoscopic devices were annealed in air and obtained 13 % enhancement in PCE, when compared to annealing in vacuum. This shows that planar devices are more prone to ambient conditions. Solar cells from some ETLs fabricated at TUT were built in glove box during Dr. Vivo's research visit to University of Cologne. The best devices fabricated in glove box showed a PCE of 20.62 %, an excellent FF of 73.50 %, 25.32 mA/cm$_2$ J_{sc}, and 1.11 V V_{oc}. These results are similar to state-of-the-art PSCs, and prove that the fabrication conditions of the ETL have no influence on the cell performance. The cells fabricated in ambient air show clearly decreased efficiency compared to cells fabricated in glove box. The crucial step in the PSC fabrication is evidently the fabrication of the perovskite layer. However, the results in ambient air can be improved by optimizing the fabrication process as well as the cell structure.

The cells with triple cation perovskite showed a good stability over a time period of 500 hours. The ageing tests showed increased PCEs, FFs, J_{sc} and V_{oc}, for both planar and mesoscopic devices, when the samples were restored in dark. For example, after 150 hours of restoring, the PCE, FF, and J_{sc}, for planar device, had increased 13.7 %, 13.4 %, and 3.6 %, respectively. On the other hand, V_{oc} showed a modest decrease by 2.5 %. This remarkable phenomenon for PSCs has been also recently reported in literature, even though the mechanism behind it has not been explained yet. This phenomenon could imply that PSCs are able to recover during the day and night cycles in their natural working conditions.

All the best performing samples were fabricated with TiO_2 ETL instead of SnO_2 ETL. The best performing devices with SnO_2 ETL showed 0.47 % and 4.60 % PCE for planar and mesoscopic cell architectures, respectively. The worse cell performance of the devices with SnO_2 ETL can be attributed to the abundance of pinholes observed in the spin coated SnO_2 layer. The spin coated TiO_2 layer showed reduced amount of pinholes and in spray pyrolyzed TiO_2 layer no pinholes were observed. The TiO_2 layers were also observed have a uniform thickness distribution compared to SnO_2 layer. This has a negative influence on the charge transfer.

The results of this Thesis meet the set targets of developing PSCs with good efficiency and great stability, fabricated in ambient conditions. The results demonstrate that it is possible to fabricate PSCs with relatively high efficiency in ambient conditions. One of the parameters hindering the higher efficiencies is the J_{sc}, which might be enhanced by optimizing the device structure and with alternative fabrication methods. Also higher Cs concentrations in the triple cation perovskite should be studied in ambient conditions. The phenomenon of enhancing cell parameters, when the cells are restored in dark, should be studied in more detail, for example by X-ray diffraction and absorption spectroscopy.

REFERENCES

[1] B.P. Rand, H. Richter, Organic Solar Cells: Fundamentals, Devices, and Up-scaling, 1st ed. CRC Press, Florida, 2014, 810 p.

[2] J. Cui, H. Yuan, J. Li, X. Xu, Y. Shen, H. Lin, M. Wang, Recent Progress in Efficient Hybrid Lead Halide Perovskite Solar Cells, Science and Technology of Advanced Materials, Vol. 16, Iss. 3, 2015, pp. 36004.

[3] S. Collavini, S.F. Völker, J.L. Delgado, Understanding the Outstanding Power Conversion Efficiency of Perovskite-Based Solar Cells, Angew. Chem. Int. Ed., Vol. 54, Iss. 34, 2015, pp. 9757−9759.

[4] NREL, Best Research-Cell Efficiencies, https://www.nrel.gov/pv/assets/images/efficiency-chart.png. (Retrieved 20.02.2017)

[5] A. Reinders, P. Verlinden, A. Freundlich, W. van Sark, Photovoltaic Solar Energy: From Fundamentals to Applications, 1st ed. John Wiley & Sons, Chichester, 2017, 720 p.

[6] T. Engel, P. Reid, Physical Chemistry, Pearson, San Fancisco, 2005, 1061 p.

[7] K. Mertens, Photovoltaics: Fundamentals, Technology and Practice, 1st ed. Wiley, Munich, 2014, 297 p.

[8] N. Park, M. Grätzel, T. Miyasaka, Organic-Inorganic Halide Perovskite Photovoltaics: From Fundamentals to Device Architectures, Springer, 2016, 364 p.

[9] A. McEvoy, L. Castaner, T. Markvart, Solar Cells: Materials, Manufacture and Operation, 2nd ed. Academic Press, GB, 2013, 655 p.

[10] S. Collavini, S.F. Völker, J.L. Delgado, Understanding the Outstanding Power Conversion Efficiency of Perovskite-Based Solar Cells, Angew. Chem. Int. Ed., Vol. 54, Iss. 34, 2015, pp. 9757−9759.

[11] H. Zhou, Q. Chen, G. Li, S. Luo, T. Song, H. Duan, Z. Hong, J. You, Y. Liu, Y. Yang, Interface Engineering of Highly Efficient Perovskite Solar Cells, Science, Vol. 345, Iss. 6196, 2014, pp. 542−546.

[12] M. Wright, A. Uddin, Organic-Inorganic Hybrid Solar Cells: A Comparative Review, Solar Energy Materials & Solar Cells, Vol. 107, 2012, pp. 87-111.

[13] B. Qi, J. Wang, Fill Factor in Organic Solar Cells, Phys. Chem. Chem. Phys., Vol. 15, Iss. 23, 2013, pp. 8972−8982.

[14] B. Qi, J. Wang, Open-Circuit Voltage in Organic Solar Cells, J. Mater. Chem., Vol. 22, Iss. 46, 2012, pp. 24315–24325.

[15] J.P. Correa-Baena, L. Steier, W. Tress, M. Saliba, S. Neutzner, T. Matsui, F. Giordano, J. Jacobsson, A.J.S. Kandada, S.M. Zakeeruddin, A. Petrozza, A. Abate, M.K. Nazeeruddin, M. Grätzel, A. Hagfeldt, Highly Efficient Planar Perovskite Solar Cells Through Band Alignment Engineering, Energy Environ. Sci., Vol. 8, 2015, pp. 2928−2934.

[16] P.P. Boix, S. Agarwala, T.M. Koh, N. Mathews, S.G. Mhaisalkar, Perovskite Solar Cells: Beyond Methylammonium Lead Iodide, J. Phys. Chem. Lett., Vol. 6, Iss. 5, 2015, pp. 898–907.

[17] D. Wang, M. Wright, N.K. Elumalai, A. Uddin, Stability of Perovskite Solar Cells, Solar Energy Materials and Solar Cells, Vol. 147, 2016, pp. 255−275.

[18] R.J.D. Tilley, Perovskites: Structure-Property Relationships, 1st ed. Wiley, Chicester, 2016, 330 p.

[19] A.J. Nozik, G. Conibeer, M.C. Beard, Advanced Concepts in Photovoltaics, Royal Society of Chemistry, Cambridge, 2014, 608 p.

[20] T.C. Sum, N. Matthews, Advancements in Perovskite Solar Cells: Photophysics Behind the Photovoltaics, Energy Environ. Sci., Vol. 7, 2014, pp. 2518−2534.

[21] C. Motta, F. El-Mellouhi, S. Kais, N. Tabet, F. Alharbi, S. Sanvito, Revealing the Role of Organic Cations in Hybrid Halide Perovskite $CH_3NH_3PbI_3$, Nature communications, Vol. 6, 2015, pp. 7026−7033.

[22] C. Bi, Q. Wang, Y. Shao, Y. Yuan, Z. Xiao, J. Huang, Non-Wetting Surface-Driven High-Aspect-Ratio Crystalline Grain Growth for Efficient Hybrid Perovskite Solar Cells, Nature communications, Vol. 6, 2015, pp. 7747−7754.

[23] G. Kieslich, S. Sun, A.K. Cheetham, Solid-State Principles Applied to Organic–Inorganic Perovskites: New Tricks for an Old Dog, Chem. Sci., Vol. 5, Iss. 12, 2014, pp. 4712–4715.

[24] N.J. Jeon, J.H. Noh, W.S. Yang, Y.C. Kim, S. Ryu, J. Seo, S.I. Seok, Compositional Engineering of Perovskite Materials for High-Performance Solar Cells, Nature, Vol. 517, Iss. 7535, 2015, pp. 476−490.

[25] M. Saliba, T. Matsui, J.Y. Seo, K. Domanski, J.P. Correa-Baena, M.K. Nazeeruddin, S.M. Zakeeruddin, A. Abate, A. Hagfeldt, M. Grätzel, Cesium-Containing Triple Cation Perovskite Solar Cells: Improved Stability, Reproducibility and High Efficiency, Energy Environ. Sci., Vol. 9, 2016, pp. 1989−1997.

[26] J. Qing, H. Chandran, Y. Cheng, S. Tsang, M. Lo, C. Lee, Low Temperature Fabrication of Formamidinium Based Perovskite Solar Cells with Enhanced Performance by Chlorine Incorporation, Organic Electronics, Vol. 38, 2016, pp. 144−149.

[27] M. Saliba, T. Matsui, K. Domanski, J.-. Seo, A. Ummadisingu, S.M. Zakeeruddin, J.-. Correa-Baena, W.R. Tress, A. Abate, A. Hagfeldt, M. Gratzel, Incorporation of Rubidium Cations into Perovskite Solar Cells Improves Photovoltaic Performance, Science, Vol. 354, Iss. 6309, 2016, pp. 206−209.

[28] C.C. Stoumpos, C.D. Malliakas, J.A. Peters, Z. Liu, M. Sebastian, J. Im, T.C. Chasapis, A.C. Wibowo, D.Y. Chung, A.J. Freeman, B.W. Wessels, M.G. Kanatzidis, Crystal Growth of the Perovskite Semiconductor $CsPbBr_3$: A New Material for High-Energy Radiation Detection, Crystal Growth and Design, Vol. 13, Iss. 7, 2013, pp. 2722−2727.

[29] N. Park, Perovskite Solar Cells: An Emerging Photovoltaic Technology, Materials Today, Vol. 18, Iss. 2, 2015, pp. 65-72.

[30] I. Borriello, G. Cantele, D. Ninno, Ab Initio Investigation of Hybrid Organic-Inorganic Perovskites Based on Tin Halides, Physical Review B, Vol. 77, Iss. 23, 2008, .

[31] H. Choi, J. Jeong, H.B. Kim, S. Kim, B. Walker, G.H. Kim, J.Y. Kim, Cesium-Doped Methylammonium Lead Iodide Perovskite Light Absorber for Hybrid Solar Cells, Nano Energy, Vol. 7, 2014, pp. 80−85.

[32] J. Lee, D. Kim, H. Kim, S. Seo, S.M. Cho, N. Park, Formamidinium and Cesium Hybridization for Photo- and Moisture-Stable Perovskite Solar Cell, Advanced Energy Materials, Vol. 5, Iss. 20, 2015, pp. 1501310.

[33] C. Yi, J. Luo, S. Meloni, A. Boziki, N. Ashari-Astani, C. Grätzel, S.M. Zakeeruddin, U. Röthlisberger, M. Grätzel, Entropic Stabilization of Mixed A-Cation ABX_3 Metal Halide Perovskites for High Performance Perovskite Solar Cells, Vol. 9, Iss. 2, 2016, pp. 656−662.

[34] Q. Dong, J. Song, Y. Fang, Y. Shao, S. Ducharme, J. Huang, Lateral-Structure Single-Crystal Hybrid Perovskite Solar Cells via Piezoelectric Poling, Advanced Materials, Vol. 28, Iss. 14, 2016, pp. 2816−2821.

[35] Y. Lin, L. Shen, J. Dai, Y. Deng, Y. Wu, Y. Bai, X. Zheng, J. Wang, Y. Fang, H. Wei, W. Ma, X.C. Zeng, X. Zhan, J. Huang, π-Conjugated Lewis Base: Efficient Trap-Passivation and Charge-Extraction for Hybrid Perovskite Solar Cells, Advanced Materials, Vol. 29, Iss. 7, 2017, pp. 1604545.

[36] G. Yang, H. Tao, P. Qin, W. Ke, G. Fang, Recent Progress in Electron Transport Layers for Efficient Perovskite Solar Cells, J. Mater. Chem. A, Vol. 4, Iss. 11, 2016, pp. 397−399.

[37] E.H. Anaraki, A. Kermanpur, L. Steier, K. Domanski, T. Matsui, W. Tress, M. Saliba, A. Abate, M. Grätzel, A. Hagfeldt, J. Correa-Baena, Highly Efficient and Stable Planar Perovskite Solar Cells by Solution-Processed Tin Oxide, Energy Environ.Sci, Vol. 9, Iss. 10, 2016, pp. 3128−3134.

[38] L. Filipovic, S. Selberherr, G.C. Mutinati, E. Brunet, S. Steinhauer, A. Kock, J. Teva, J. Kraft, J. Siegert, F. Schrank, Methods of Simulating Thin Film Deposition Using Spray Pyrolysis Techniques, Microelectronic Engineering, Vol. 117, 2014, pp. 57−66.

[39] M. Liu, M.B. Johnston, H.J. Snaith, Efficient Planar Heterojunction Perovskite Solar Cells by Vapour Deposition, Nature, Vol. 501, Iss. 7467, 2013, pp. 395−398.

[40] N.J. Jeon, J.H. Noh, Y.C. Kim, W.S. Yang, S. Ryu, S. Il Seok, Solvent Engineering for High-Performance Inorganic-Organic Hybrid Perovskite Solar Cells, Nature Materials, Vol. 13, Iss. 9, 2014, pp. 897−903.

[41] D. Bi, C. Yi, J. Luo, J. Décoppet, F. Zhang, S. Zakeeruddin, X. Li, A. Hagfeldt, M. Grätzel, Polymer-Templated Nucleation and Crystal Growth of Perovskite Films for Solar Cells with Efficiency Greater Than 21 %, Nature Energy, Vol. 1, Iss. 10, 2016, pp. 16142.

[42] J. Burschka, N. Pellet, S. Moon, R. Humphry-Baker, P. Gao, M.K. Nazeeruddin, M. Grätzel, Sequential Deposition as a Route to High-Performance Perovskite-Sensitized Solar Cells, Nature, Vol. 499, Iss. 7458, 2013, pp. 316−319.

[43] R.S. Sanchez, E. Mas-Marza, Light-Induced Effects on Spiro-OMeTAD Films and Hybrid Lead Halide Perovskite Solar Cells, Solar Energy Materials and Solar Cells, Vol. 158, 2016, pp. 189−194.

[44] Y. Yue, N. Salim, Y. Wu, X. Yang, A. Islam, W. Chen, J. Liu, E. Bi, F. Xie, M. Cai, L. Han, Enhanced Stability of Perovskite Solar Cells through Corrosion-Free Pyridine Derivatives in Hole-Transporting Materials, Advanced Materials, Vol. 28, Iss. 48, 2016, pp. 10738−10743.

[45] I.M. Ahmed, A. Habib, S.S. Javaid, Perovskite Solar Cells: Potentials, Challenges, and Opportunities, International Journal of Photoenergy, 2015, pp. 781-793.

[46] J. You, L. Meng, T. Song, T. Guo, M.Y. Yang, W. Chang, Z. Hong, H. Chen, H. Zhou, Q. Chen, Y. Liu, N. De Marco, Y. Yang, Improved Air Stability of Perovskite Solar Cells Via Solution-Processed Metal Oxide Transport Layers, Nature Nanotechnology, Vol. 11, Iss. 1, 2016, pp. 75-81.

[47] J. Cha, J. Lee, D. Son, H. Kim, I. Jang, N. Park, Mesoscopic Perovskite Solar Cells with an Admixture of Nanocrystalline TiO_2 and Al_2O_3: Role of Interconnectivity of TiO_2 in Charge Collection, Nanoscale, Vol. 8, Iss. 12, 2016, pp. 6341−6351.

[48] A.R. Pascoe, M. Yang, N. Kopidakis, K. Zhu, M.O. Reese, G. Rumbles, M. Fekete, N.W. Duffy, Y. Cheng, Planar Versus Mesoscopic Perovskite Microstructures: The Influence of $CH_3NH_3PbI_3$ Morphology on Charge Transport and Recombination Dynamics, Nano Energy, Vol. 22, 2016, pp. 439-452.

[49] C. Wang, D. Zhao, C.R. Grice, W. Liao, Y. Yu, A. Cimaroli, N. Shrestha, P.J. Roland, J. Chen, Z. Yu, P. Liu, N. Cheng, R.J. Ellingson, X. Zhao, Y. Yan, Low-Temperature Plasma-Enhanced Atomic Layer Deposition of Tin Oxide Electron Selective Layers

for Highly Efficient Planar Perovskite Solar Cells, J. Mater. Chem. A, Vol. 4, 2016, pp. 12080−12087.

[50] Z. Wang, Z. Shi, T. Li, Y. Chen, W. Huang, Stability of Perovskite Solar Cells: A Prospective on the Substitution of the A Cation and X Anion, Angewandte Chemie International Edition, Vol. 56, Iss. 5, 2017, pp. 1190−1212.

[51] B. Wu, K. Fu, N. Yantara, G. Xing, S. Sun, T.C. Sum, N. Mathews, Charge Accumulation and Hysteresis in Perovskite-Based Solar Cells: An Electro-Optical Analysis, Adv. Energy Mater., Vol. 5, Iss. 19, 2015, pp. 1500829.

[52] H. Yoon, S.M. Kang, J.K. Lee, M. Choi, Hysteresis-Free Low-Temperature-Processed Planar Perovskite Solar Cells with 19.1% Efficiency, Energy Environ. Sci., Vol. 9, Iss. 7, 2016, pp. 2262−2266.

[53] P. Vivo, A. Ojanpera, J.H. Smatt, S. Sanden, S.G. Hashmi, K. Kaunisto, P. Ihalainen, M.T. Masood, R. Osterbacka, P.D. Lund, H. Lemmetyinen, Influence of TiO_2 Compact Layer Precursor on the Performance of Perovskite Solar Cells, Organic Electronis, Vol. 41, 2017, pp. 287−293.

[54] Dyesol Ltd. http://www.dyesol.com/. (Retrieved 20.03.2017)

[55] J.A. Christians, J.S. Manser, P.V. Kamat, Best Practices in Perovskite Solar Cell Efficiency Measurements. Avoiding the Error of Making Bad Cells Look Good, J. Phys. Chem. Lett., Vol. 6, Iss. 5, 2015, pp. 852−857.

[56] J.I. Goldstein, D.C. Joy, D.E. Newbury, Scanning Electron Microscopy and X-ray Microanalysis, 3rd ed. Springer US, New York, 2003, 689 p.

[57] Y. Jiang, E.J. Juarez-Perez, Q. Ge, S. Wang, M.R. Leyden, L.K. Ono, S.R. Raga, J. Hu, Y. Qi, Post-Annealing of $MAPbI_3$ Perovskite Films with Methylamine for Efficient Perovskite Solar Cells, Materials Horizons, Vol. 3, Iss. 6, 2016, pp. 548−555.

[58] J. Yin, J. Cao, X. He, S.F. Yuan, S.B. Sun, J. Li, N.F. Zheng, L.W. Lin, Improved Stability of Perovskite Solar Cells in Ambient Air by Controlling the Mesoporous layer, Journal of Materials Chemistry A, Vol. 3, Iss. 32, 2015, pp. 16860−16866.

[59] Q.D. Tai, P. You, H.Q. Sang, Z.K. Liu, C.L. Hu, H. Chan, F. Yan, Efficient and Stable Perovskite Solar Cells Prepared in Ambient Air Irrespective of the Humidity, Nature Communications, Vol. 7, 2016, pp. 11105.

[60] H. Sarvari, X. Wang, Y. Wang, P. Zhang, S. Li, H. Dang, V.P. Singh, Z. Chen, Comprehensive Study of the Two-Step Solution Processes in Ambient Air for Lead Iodide Perovskite Solar Cells, 2016 IEEE 43rd Photovoltaic Specialists Conference (PVSC), IEEE, pp. 0823−0827.

[61] G. Wang, D. Liu, J. Xiang, D. Zhou, K. Alameh, B. Ding, Q. Song, Efficient Perovskite Solar Cell Fabricated in Ambient Air Using One-Step Spin-Coating, Vol. 6, Iss. 49, 2016, pp. 43299−4333.

[62] J. Kim, H.P. Kim, M. Teridi, A.B. Yusoff, J. Jang, Bandgap Tuning of Mixed Organic Cation Utilizing Chemical Vapor Deposition Process, Scientific Reports, Vol. 6, 2016, pp. 37378−37389.

[63] K. Sveinbjornsson, K. Aitola, J.B. Zhang, M.B. Johansson, X.L. Zhang, J.P. Correa-Baena, A. Hagfeldt, G. Boschloo, E. Johansson, Ambient Air-Processed Mixed-Ion Perovskites for High-Efficiency Solar Cells, Journal of Materials Chemistry A, Vol. 4, Iss. 42, 2016, pp. 16536−16545.

[64] F. Huang, L. Jiang, A.R. Pascoe, Y. Yan, U. Bach, L. Spiccia, Y. Cheng, Fatigue Behavior of Planar $CH_3NH_3PbI_3$ Perovskite Solar Cells Revealed by Light on/off Diurnal Cycling, Nano Energy, Vol. 27, 2016, pp. 509−514.

Table *Best performing cells measured in light with forward scan. Triple cation perovskite indicates Cs/MA/FA triple cation perovskite, SC means spin coating, CBD chemical bath deposition, cl. is the ETL compact layer and mp. indicates the mesoporous layer.*

Cell Structure	Method of perovskite fabrication, annealing	Method of ETL fabrication	Scan direction	PCE [%]	FF [%]	J_{sc} [mA/cm^2]	V_{oc} [V]
FTO|TiO2 cl.|MAPbI3|spiro|Au	1-step, vacuum	SC	forward	3,8949	46,8219	9,0418	0,9200
			reverse	3,5233	50,8927	7,7787	0,8900
FTO|SnO2 cl.|MAPbI3|spiro|Au	1-step, vacuum	SC	forward	0,4666	41,3488	4,2571	0,2651
			reverse	0,0563	39,2664	1,2521	0,1145
FTO|SnO2 cl.|MAPbI3|spiro|Au	1-step, vacuum	SC+CBD	forward	0,0111	39,5062	0,1045	0,2700
			reverse	0,0113	29,4118	0,2265	0,1700
FTO|TiO2 cl.|MAPbI3|spiro|Au	1-step, air	SC	forward	1,6685	39,5462	5,4695	0,7714
			reverse	1,2689	51,1775	3,2142	0,7714
FTO|SnO2 cl.|MAPbI3|spiro|Au	1-step, air	SC	forward	0,3018	33,9926	2,4208	0,3667
			reverse	0,0195	27,1008	1,6761	0,0429
FTO|TiO2 cl.|TiO2 mp. (30 NR-D)|MAPbI3|spiro|Au	2-steps, vacuum	SC	forward	4,1519	55,1894	8,4036	0,8952
			reverse	3,7524	67,7763	6,7974	45,0000
FTO|SnO2 cl.|TiO2 mp.(30 NR-D)|MAPbI3|spiro|Au	2-steps, vacuum	SC	forward	2,3000	37,9660	8,7353	0,6935
			reverse	3,7008	45,8040	9,4522	0,8548
FTO|TiO2 cl.|TiO2 mp. (18 NR-T)|MAPbI3|spiro|Au	1-step, air	SC	forward	0,9967	55,2676	2,7744	0,6500
			reverse	0,1693	22,5502	1,5385	0,4881
FTO|TiO2 cl.|TiO2 mp. (30 NR-D)|MAPbI3|spiro|Au	1-step, air	SC	forward	0,9246	54,9220	2,4381	0,6905
			reverse	0,0901	31,2183	0,8844	0,3262
FTO|TiO2 cl.|(triple cation perovskite)|spiro|Au	1-step, vacuum	SC	forward	5,6997	64,0689	12,8279	0,6935
			reverse	9,8773	60,5088	14,8831	1,0968
FTO|SnO2 cl.|(triple cation perovskite)|spiro|Au	1-step, vacuum	SC	forward	3,0418	41,9182	6,8685	1,0565
			reverse	4,5983	59,7907	8,2209	0,9355
FTO|SnO2 cl.| TiO2 mp.(30 NR-D)|(triple cation perovskite)|spiro |Au	1-step, vacuum	SC	forward	1,0442	41,9299	9,9615	0,2500
			reverse	0,9625	43,2120	8,9098	0,2500
FTO|TiO2 cl.|TiO2 mp.(30 NR-D)|(triple cation perovskite)|spiro |Au	1-step, vacuum	SC	forward	6,4590	57,7273	14,4521	0,7742
			reverse	5,3781	53,4530	12,9965	0,7742
FTO|TiO2 cl.|TiO2 mp.(18 NR-T)|(triple cation perovskite)|spiro |Au	1-step, N2	SC	forward	5,7121	61,2883	11,4428	0,8145
			reverse	4,3842	58,1762	9,7340	0,7742

APPENDIX A: BEST PERFORMING CELLS

Cell Structure	Method of perovskite fabrication, annealing	Method of ETL fabrication	Scan direction	PCE [%]	FF [%]	J_{sc} [mA/cm^2]	V_{oc} [V]
FTO | TiO2 cl. | TiO2 mp.(18 NR-T) | (triple cation perovskite) | spiro | Au	1-step, air	SC	forward	4,4914	60,9306	8,6477	0,8524
			reverse	2,8611	64,3756	5,4741	0,8119
FTO | TiO2 cl. | TiO2 mp.(30 NR-D) | (triple cation perovskite) | spiro | Au	1-step, air	SC	forward	7,3837	66,4961	12,4090	0,8952
			reverse	7,0718	65,4636	12,0672	0,8952
FTO | TiO2 cl. | (triple cation perovskite) | spiro | Au	1-step, air	spray pyrolysis	forward	6,0422	40,4439	15,3417	0,9738
			reverse	7,9402	54,5120	14,9579	0,9738
FTO | TiO2 cl. | TiO2 mp.(18 NR-T) | (triple cation perovskite) | spiro | Au	1-step, air	spray pyrolysis	forward	4,2980	58,6375	9,0279	0,8119
			reverse	3,3361	76,4943	5,6536	0,7714
FTO | TiO2 cl. | TiO2 mp.(30 NR-D) | (triple cation perovskite) | spiro | Au	1-step, air	spray pyrolysis	forward	5,4199	55,0378	11,5529	0,8524
			reverse	2,6344	55,1614	5,8822	0,8119